Physics of Fluids

Boundary integral simulations of a red blood cell squeezing through a submicron slit under prescribed inlet and outlet pressures

Cite as: Phys. Fluids **31**, 031902 (2019); https://doi.org/10.1063/1.5081057
Submitted: 13 November 2018 . Accepted: 09 January 2019 . Published Online: 08 March 2019

Huijie Lu (卢慧杰), and Zhangli Peng (彭张立)

Physics of Fluids ARTICLE scitation.org/journal/phf

Boundary integral simulations of a red blood cell squeezing through a submicron slit under prescribed inlet and outlet pressures

Cite as: Phys. Fluids 31, 031902 (2019); doi: 10.1063/1.5081057
Submitted: 13 November 2018 • Accepted: 9 January 2019 •
Published Online: 8 March 2019

Huijie Lu (卢慧杰) and Zhangli Peng (彭张立)

AFFILIATIONS

Department of Aerospace and Mechanical Engineering, University of Notre Dame, Notre Dame, Indiana 46556-5637, USA

ABSTRACT

We developed a boundary integral formulation to simulate a red blood cell (RBC) squeezing through a submicron slit under prescribed inlet and outlet pressures. The main application of this computational study is to investigate splenic filtrations of RBCs and the corresponding *in vitro* mimicking microfluidic devices, during which RBCs regularly pass through inter-endothelial slits with a width less than 1.0 μm. The diseased and old RBCs are damaged or destroyed in this mechanical filtration process. We first derived the boundary integral equations of a RBC immersed in a confined domain with prescribed inlet and outlet pressures. We applied a unified self-adaptive quadrature to accurately evaluate singular and nearly singular integrals, which are especially important in this fluid-structure interaction problem with strong lubrication. A multiscale model is applied to calculate forces from the RBC membrane, and it is coupled to boundary integral equations to simulate the fluid-structure interaction. After multi-step verifications and validations against analytical and experimental results, we systematically investigated the effects of pressure drop, volume-to-surface-area ratio, internal viscosity, and membrane stiffness on RBC deformation and internal stress. We found that spectrins of RBCs could be stretched by more than 2.5 times under high hydrodynamic pressure and that the bilayer tension could be more than 500 pN/μm, which might be large enough to open mechanosensitive channels but too small to rupture the bilayer. On the other hand, we found that the bilayer-cytoskeletal dissociation stress is too low to induce bilayer vesiculation.

I. INTRODUCTION

Numerical simulations of vesicles, elastic capsules, and red blood cells (RBCs) in various flows are mathematically fascinating due to their multiphysics fluid-structure interactions and simplicities of flow fields and membrane structures.[1–3] These simulations have also proved to be useful in applications such as the design of microfluidic devices, study of microcirculation physiology[4,5] and hemorheology,[6] and design of artificial capsules with controlled release of substance in pharmaceutical, cosmetic, and food industries.[1] They are mathematically simpler than general fluid-structure interaction problems because the flows are usually laminar, in most cases Stokes flows without the effect of inertia forces. Furthermore, compared to most eukaryotic cells, elastic capsules and vesicles have much simpler structures without internal organelles so that they can be modeled accurately using continuum theories. The RBC is an exception in eukaryotic cells and is similar to an elastic capsule. However, their numerical simulations are still challenging due to the elastic interfaces with strain-dependent and rate-dependent in-plane and bending properties. The existing commercial simulation packages still cannot capture the fluid-structure interaction of these sharp and complicated 3D interfaces accurately. Development of efficient, accurate, and robust numerical algorithms to simulate cells, elastic capsules, and vesicles in flows might have significant impacts on the future biomedical industry related to lab-on-a-chip technologies and artificial capsules. Computational modeling can provide important information such as stress distribution on the capsules and vesicles when they pass through microfluidic devices and deformation of RBCs in microcirculation, which are extremely difficult to measure in experiments.

There are three major groups of numerical methods in the existing literature to study motion and deformation of elastic capsules and RBCs in flows.[1–3] In the first group, boundary integral equations are used to represent the Stokes flow and coupled to the membrane,[7–9] which is usually modeled as meshes or spectral elements[10] either by enforcing the membrane equilibrium equation directly at the local grid points[8] or by the finite element method based on the principle of virtual work.[7,11] This type of method has been known to be very precise in various studies of simple shear flow and plane hyperbolic flow.[1,2] In the second group of the immerse-boundary type methods, the fluid domain is solved using either finite difference methods,[12–14] finite element methods,[15] finite volume methods, or lattice Boltzmann methods,[16] and the capsule membrane is solved using continuum methods such as the finite element method. The forces from capsule membrane nodes are distributed to the fluid domain as Dirac delta functions, which are approximated by smooth functions sharply varying over a few fixed grid cells. Although this approximation may decrease the accuracy of capturing the sharp interfaces, it enables these methods to include the inertial forces by solving the Navier-Stokes equation, which is missing in boundary integral formulations of Stokes flows. In the third group, particle methods such as dissipative particle dynamics (DPD),[17,18] multi-particle collision dynamics,[19] and smoothed particle hydrodynamics (SPH)[20] are used. Bounce-back algorithms and repulsive interactions are employed to enforce the boundary conditions on the interfaces.[17] Capsule and RBC membranes are modeled as triangular networks of particles with bond, angle, and dihedral interactions.[21] In addition to these three groups, phase-field methods[22] and the arbitrary Lagrangian Eulerian (ALE) method using the finite element method[23,24] are used as well to study capsules and vesicles in flows.

Recently the mechanical filtration of RBCs in the spleen and the corresponding *in vitro* microfluidic studies received a lot of attention.[25–32] Because the inter-endothelial slit in the spleen is the place where RBCs experience the most severe deformation, slight changes of RBC structures can lead to huge deformation differences so that it provides an ideal case to study aging and diseased RBCs.[33] Furthermore, splenic filtration of RBCs plays an important role in diseases such as malaria,[34] sickle cell disease,[35] and hereditary spherocytosis.[28,35] Simulations of RBCs passing through splenic slits were explored by various computational methods. Freund applied the boundary integral method to simulate a RBC passing through an infinitely long slit with periodic boundary conditions and constant far field velocity.[30] Salehyar *et al.* applied the boundary integral method with a multiscale model to study the transit time and bilayer-cytoskeletal separation of RBCs during splenic passage.[31,32,36] Using DPD, we also studied this process and explored the cause of linear volume-area relationship of RBC populations.[25] Recently, Li *et al.*[27] applied the coarse-grained molecular dynamics (CGMD) method to investigate RBCs with hereditary disorders in the splenic filtration process. In addition, experimental tools including microfluidic slit devices,[26] microsphere filtration systems,[28,34,37] and *ex vivo* spleen perfusion[29,38] were applied to study the retention rates and dynamics of healthy and diseased RBCs passing through splenic slits. These experimental results provide important data for model validations.

Among these various numerical methods to simulate elastic capsules in flows, the boundary integral method is a highly competitive approach.[1,2] It has high accuracy due to its direct representation of sharp interfaces and its usage of analytical fundamental solutions in terms of Green's functions. It is also highly efficient and robust due to its lack of domain meshes. But there are still several challenges to overcome for the boundary integral simulations of elastic capsules in microfluidics and microcirculations, especially when the channels are extremely narrow. First, an elastic capsule in a channel flow has been studied using the boundary integral method, but in most cases, only for the Dirichlet boundary condition of a prescribed inflow velocity or flow rate.[30,31,39–42] For example, Pozrikidis developed a three-dimensional approach to study a capsule in a tube flow, but a constant flow rate is assumed and the capsule is assumed to be far away from the wall and the inlet/outlet.[39] In many microfluidic devices, it is easier to control the pressure drop instead of the flow rate. Even in flow rate controlling devices, the pressure drop P as shown in Fig. 1 is usually constant for local individual channels. More importantly, it is most likely that the pressure drop is constant across the splenic slits in the *in vivo* condition instead of the flow rate. Barthes-Biesel and co-workers investigated the passage of an initially spherical capsule through an axisymmetric hyperbolic constriction under either constant pressure drop or constant flow rate conditions.[43–45] Therefore, there is an urgent need to consider the general Neumann boundary conditions of prescribed inlet and outlet pressures appropriately in the boundary integral formulation of capsules in three-dimensional flows. Second, the microfluidic channels or the confined spaces in the microcirculation are extremely narrow in many applications, even less than 1 μm as shown in Fig. 1 so that strong lubrication between the capsules and the channel walls can happen, which requires special numerical algorithms to accurately calculate the nearly singular integrals between the capsule and the walls. Our current study in this paper will

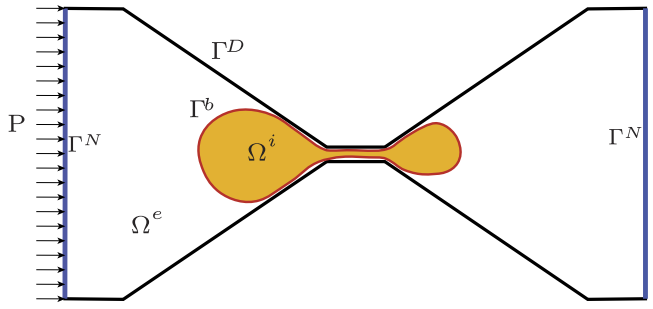

FIG. 1. Sketch of the boundary value problem and boundary conditions of an elastic capsule squeezing through a narrow channel. P is the pressure applied on the inlet, and the pressure on the outlet is zero. The fluid viscosity η_1 outside the capsule (Ω^e) might be different from the fluid viscosity η_2 inside the capsule (Ω^i).

address these important issues in boundary integral simulations of elastic capsules and vesicles in narrow channels in microfluidics and microcirculation.

II. PROBLEM DESCRIPTION AND MATHEMATICAL FORMULATION

Consider the boundary value problem of surrounding flow fields of an elastic capsule such as a red blood cell (RBC) immersed in a three-dimensional confined Stokes flow, as shown in Fig. 1. The flow can be described by the Stokes equation and the continuity equation as

$$\eta \nabla^2 \mathbf{u} = \nabla p, \tag{1}$$

$$\nabla \cdot \mathbf{u} = 0, \tag{2}$$

where $\mathbf{u}$ is the flow velocity, η is the dynamic viscosity ($\eta = \eta_1$ in Ω^e and $\eta = \eta_2$ in Ω^i), and ∇p is the pressure gradient. We denote the elastic capsule interface as Γ^b, the wall Dirichlet boundary as Γ^D, and the inlet/outlet Neumann boundary as Γ^N. On Γ^D, the flow velocity $\mathbf{u}$ is prescribed. It is zero for fixed walls, but can be specific values for prescribed velocities or flow rates. The traction on Γ^D is unknown and needs to be solved. On Γ^N, the traction including pressure is prescribed, but the velocity on Γ^N is unknown and needs to be solved. On Γ^b, the traction discontinuity is calculated from the membrane mechanics based on the membrane deformation such as using the finite element method, but the velocity is unknown and needs to be solved in the boundary integral simulations.

In most existing boundary integral simulations of elastic capsules in confined spaces, only Dirichlet boundary conditions on the inlet/outlet are considered,[30,31,39–42] or Neumann boundaries are usually replaced by Dirichlet boundaries with prescribed velocities. For example, Pozrikidis[39] assumed a constant flow rate on the tube inlet/outlet and Barthes-Biesel[43,44] used the computed transient additional pressure drop due to the capsule to convert a constant pressure problem to a prescribed flow rate problem. Therefore, a boundary integral formulation with Neumann boundary conditions on the inlet/outlet would be greatly helpful. Furthermore, in most studies, the capsules are assumed to be far away from the channel walls.[39] But in many applications, the slits in the microfluidics and microcirculation are extremely narrow, even less than 1 μm, such as the splenic filtration of RBCs and extravasation of cancer cells through inter-endothelial slits of blood vessel walls. Therefore, special numerical algorithms are required to accurately capture the strong lubrication between the capsules and the channel walls. These critical issues will be addressed in Secs. III and IV.

III. BOUNDARY INTEGRAL FORMULATION OF ELASTIC CAPSULES IN CONFINED SPACES WITH NEUMANN AND DIRICHLET BOUNDARY CONDITIONS

A. Boundary integral representation of the velocity field in the fluid domain

By applying the Lorentz reciprocal theorem,[8] the boundary integral representation of the velocity for a point $\mathbf{x}_0$ in the domain Ω^e between the bilayer Γ^b (interface), the wall Γ^D (Dirichlet boundary), and the inlet/outlet Γ^N (Neumann boundary) is given as

$$\begin{aligned} u_j(\mathbf{x}_0) = &-\frac{1}{8\pi\eta_1}\int_{\Gamma^b} \Delta f_i(\mathbf{x}) G_{ij}(\mathbf{x},\mathbf{x}_0) d\Gamma(\mathbf{x}) \\ &+ \frac{1-\lambda}{8\pi}\int_{\Gamma^b} u_i(\mathbf{x}) T_{ijk}(\mathbf{x},\mathbf{x}_0) n_k(\mathbf{x}) d\Gamma(\mathbf{x}) \\ &- \frac{1}{8\pi\eta_1}\int_{\Gamma^D} f_i^{(D)}(\mathbf{x}) G_{ij}(\mathbf{x},\mathbf{x}_0) d\Gamma(\mathbf{x}) \\ &+ \frac{1}{8\pi}\int_{\Gamma^D} u_i(\mathbf{x}) T_{ijk}(\mathbf{x},\mathbf{x}_0) n_k(\mathbf{x}) d\Gamma(\mathbf{x}) \\ &- \frac{1}{8\pi\eta_1}\int_{\Gamma^N} f_i^{(N)}(\mathbf{x}) G_{ij}(\mathbf{x},\mathbf{x}_0) d\Gamma(\mathbf{x}) \\ &+ \frac{1}{8\pi}\int_{\Gamma^N} u_i(\mathbf{x}) T_{ijk}(\mathbf{x},\mathbf{x}_0) n_k(\mathbf{x}) d\Gamma(\mathbf{x}), \end{aligned} \tag{3}$$

where the viscosity ratio $\lambda \equiv \eta_2/\eta_1$. η_1 is the fluid viscosity in the domain Ω^e, and η_2 is the fluid viscosity in the domain Ω^i. $\Delta\mathbf{f}$ is the discontinuity of the surface traction across the bilayer interface Γ^b. $\mathbf{f}^{(D)}$ is the traction on the wall Γ^D. $\mathbf{f}^{(N)}$ is the traction on the inlet/outlet Γ^N, which can be prescribed as inflow and outflow pressures if no tangential traction. The unit normal vector $\mathbf{n}$ points toward the fluid domain Ω^e. The velocity and stress Green's functions of free space Stokes flow are given by

$$G_{ij}(\mathbf{x},\mathbf{x}_0) = \frac{\delta_{ij}}{|\mathbf{x}-\mathbf{x}_0|} + \frac{(x_i - x_{0_i})(x_j - x_{0_j})}{|\mathbf{x}-\mathbf{x}_0|^3}, \tag{4}$$

$$T_{ijk}(\mathbf{x},\mathbf{x}_0) = -6\frac{(x_i - x_{0_i})(x_j - x_{0_j})(x_k - x_{0_k})}{|\mathbf{x}-\mathbf{x}_0|^5}, \tag{5}$$

where δ_{ij} is Kronecker's delta. Equations (4) and (5) are fundamental solutions of the Stokes equation [Eq. (1)] and the continuity equation [Eq. (2)] under a point force in the 3D infinite free space domain.

The Dirichlet boundary condition on the wall and the Neumann boundary condition on the inlet/outlet are specified as

$$\begin{aligned} \boldsymbol{u} &= \bar{\boldsymbol{u}} \quad \text{on} \quad \Gamma^D, \\ \boldsymbol{f}^{(N)} &= \bar{\boldsymbol{f}} \quad \text{on} \quad \Gamma^N. \end{aligned} \tag{6}$$

B. Boundary integral equations of the velocities on the bilayer (interface), the inlet/outlet (Neumann boundaries), and the wall (Dirichlet boundaries)

Taking the limit as the point $\mathbf{x}_0$ approaches the bilayer Γ^b from external side, since the bilayer is a Lyapunov surface, i.e., it has a continuously varying normal vector, and the velocity over the bilayer varies in a continuous manner, we have

$$\begin{aligned} \lim_{\mathbf{x}_0 \to \Gamma^b} \int_{\Gamma^b} u_i(\mathbf{x}) T_{ijk}(\mathbf{x},\mathbf{x}_0) n_k(\mathbf{x}) d\Gamma(\mathbf{x}) &= 4\pi u_j(\mathbf{x}_0) \\ &+ \int_{\Gamma^b}^{PV} u_i(\mathbf{x}) T_{ijk}(\mathbf{x},\mathbf{x}_0) n_k(\mathbf{x}) d\Gamma(\mathbf{x}), \end{aligned} \tag{7}$$

where the superscript PV denotes the principal value integral computed by placing the evaluation point $\mathbf{x}_0$ precisely on the interface Γ^b.

Substituting Eq. (7) into Eq. (3) and applying the boundary conditions of Eq. (6), we get the boundary integral equation of the velocity on the bilayer

$$\begin{aligned} u_j(\mathbf{x}_0) = &-\frac{1}{4\pi\eta_1(1+\lambda)}\int_{\Gamma^b}\Delta f_i(\mathbf{x})G_{ij}(\mathbf{x},\mathbf{x}_0)d\Gamma(\mathbf{x}) \\ &+\frac{1-\lambda}{4\pi(1+\lambda)}\int_{\Gamma^b}^{PV}u_i(\mathbf{x})T_{ijk}(\mathbf{x},\mathbf{x}_0)n_k(\mathbf{x})d\Gamma(\mathbf{x}) \\ &-\frac{1}{4\pi\eta_1(1+\lambda)}\int_{\Gamma^D}f_i^{(D)}(\mathbf{x})G_{ij}(\mathbf{x},\mathbf{x}_0)d\Gamma(\mathbf{x}) \\ &+\frac{1}{4\pi(1+\lambda)}\int_{\Gamma^D}\bar{u}_i(\mathbf{x})T_{ijk}(\mathbf{x},\mathbf{x}_0)n_k(\mathbf{x})d\Gamma(\mathbf{x}) \\ &-\frac{1}{4\pi\eta_1(1+\lambda)}\int_{\Gamma^N}\bar{f}_i(\mathbf{x})G_{ij}(\mathbf{x},\mathbf{x}_0)d\Gamma(\mathbf{x}) \\ &+\frac{1}{4\pi(1+\lambda)}\int_{\Gamma^N}u_i(\mathbf{x})T_{ijk}(\mathbf{x},\mathbf{x}_0)n_k(\mathbf{x})d\Gamma(\mathbf{x}). \end{aligned} \tag{8}$$

Now taking the limit as the point $\mathbf{x}_0$ approaches the inlet/outlet Γ^N, by using the principal value integral on the inlet/outlet and applying the boundary conditions, similarly, the boundary integral equation of the velocity on the inlet/outlet can be written as

$$\begin{aligned} u_j(\mathbf{x}_0) = &-\frac{1}{4\pi\eta_1}\int_{\Gamma^b}\Delta f_i(\mathbf{x})G_{ij}(\mathbf{x},\mathbf{x}_0)d\Gamma(\mathbf{x}) \\ &+\frac{1-\lambda}{4\pi}\int_{\Gamma^b}u_i(\mathbf{x})T_{ijk}(\mathbf{x},\mathbf{x}_0)n_k(\mathbf{x})d\Gamma(\mathbf{x}) \\ &-\frac{1}{4\pi\eta_1}\int_{\Gamma^D}f_i^{(D)}(\mathbf{x})G_{ij}(\mathbf{x},\mathbf{x}_0)d\Gamma(\mathbf{x}) \\ &+\frac{1}{4\pi}\int_{\Gamma^D}\bar{u}_i(\mathbf{x})T_{ijk}(\mathbf{x},\mathbf{x}_0)n_k(\mathbf{x})d\Gamma(\mathbf{x}) \\ &-\frac{1}{4\pi\eta_1}\int_{\Gamma^N}\bar{f}_i(\mathbf{x})G_{ij}(\mathbf{x},\mathbf{x}_0)d\Gamma(\mathbf{x}) \\ &+\frac{1}{4\pi}\int_{\Gamma^N}^{PV}u_i(\mathbf{x})T_{ijk}(\mathbf{x},\mathbf{x}_0)n_k(\mathbf{x})d\Gamma(\mathbf{x}). \end{aligned} \tag{9}$$

Similarly, when the point $\mathbf{x}_0$ lies on the wall Γ^D, the boundary integral equation of the velocity on the wall is

$$\begin{aligned} \bar{u}_j(\mathbf{x}_0) = &-\frac{1}{4\pi\eta_1}\int_{\Gamma^b}\Delta f_i(\mathbf{x})G_{ij}(\mathbf{x},\mathbf{x}_0)d\Gamma(\mathbf{x}) \\ &+\frac{1-\lambda}{4\pi}\int_{\Gamma^b}u_i(\mathbf{x})T_{ijk}(\mathbf{x},\mathbf{x}_0)n_k(\mathbf{x})d\Gamma(\mathbf{x}) \\ &-\frac{1}{4\pi\eta_1}\int_{\Gamma^D}f_i^{(D)}(\mathbf{x})G_{ij}(\mathbf{x},\mathbf{x}_0)d\Gamma(\mathbf{x}) \\ &+\frac{1}{4\pi}\int_{\Gamma^D}^{PV}\bar{u}_i(\mathbf{x})T_{ijk}(\mathbf{x},\mathbf{x}_0)n_k(\mathbf{x})d\Gamma(\mathbf{x}) \\ &-\frac{1}{4\pi\eta_1}\int_{\Gamma^N}\bar{f}_i(\mathbf{x})G_{ij}(\mathbf{x},\mathbf{x}_0)d\Gamma(\mathbf{x}) \\ &+\frac{1}{4\pi}\int_{\Gamma^N}u_i(\mathbf{x})T_{ijk}(\mathbf{x},\mathbf{x}_0)n_k(\mathbf{x})d\Gamma(\mathbf{x}). \end{aligned} \tag{10}$$

We need to solve Eqs. (8)–(10) together for the unknown velocity $\mathbf{u}$ on the bilayer interface, the unknown velocity $\mathbf{u}$ on the inlet/outlet, and the unknown traction $\mathbf{f}^{(D)}$ on the wall. The detailed procedure and algorithm to solve these coupled equations are given in Appendix A. The differences between our current formulation and existing formulations are summarized in Table I. The major difference is that we considered the combined Neumann and Dirichlet boundary conditions with prescribed pressure and velocity, while in most existing studies, only Dirichlet boundary conditions with prescribed velocity or flow rate were considered.[30,39–42]

IV. IMPORTANT NUMERICAL ISSUES OF THE BOUNDARY INTEGRAL FORMULATION

A. Singular and nearly singular integrals

To simulate a RBC squeezing through a submicron slit, it is critical to accurately evaluate the singular and nearly singular integrals to capture the strong hydrodynamic interactions between the cell and the channel boundaries. First, in the boundary integral equations of Eqs. (8)–(10), both single-layer and double-layer potential terms are singular integrals when the point $\mathbf{x}_0$ lies on the bilayer, inlet/outlet, and wall, respectively. Numerically, the contributions of connected elements to the current collocation node are singular functions,

TABLE I. Comparison of boundary integral equation (BIE) studies of RBCs/capsules in confined spaces. In addition, the membrane equilibrium is enforced by finite elements (FE) based on the principal of virtual work in the current study, while it is enforced directly at the local grid points in the other four studies listed.

BIE studies	Boundary conditions studied	Nearly singularity integration	Discretization methods
Current study	Prescribed both pressure and velocity	Third-degree polynomial self-adaptive quadrature	Bilinear quadrilateral elements (the same interpolation in FE)
Pozrikidis[39]	Prescribed velocity	The cell is far away from walls	Six node triangular elements
Freund *et al.*[10,30]	Periodic boundary condition with prescribed velocity	Special quadrature in polar coordinates	Spectral spherical harmonics
Leyrat-Maurin *et al.*[43,44]	Prescribed pressure or velocity in axisymmetric cases	Adaptive meshing in the region of high curvature	Axisymmetric line elements
Dimitrakopoulos *et al.*[40–42]	Prescribed velocity	The cell is far away from walls	Spectral quadrilateral elements

which approach infinity at the collocation node so that specially designed quadratures are needed. Second, when the cell passes through the slit, the cell membrane gets extremely close to the wall (~50 nm) so that accurate evaluation of the nearly singular integrals is crucial. Third, the cell may fold under some conditions so that the cell surface may contact itself. Therefore, a nearly singular integral is necessary for the stability and accuracy of successful simulations. In our simulations, we applied a unified self-adaptive quadrature[46] to calculate all the singular and nearly singular integrals, which is not only very effective but also useful in simplifying the numerical implementations.

For a nearly singular integral, we first define a cutoff distance between the collocation node and the element to integrate. For elements whose distances to the current collocation node are within the cutoff distance, a third-degree polynomial coordinate transformation[46] is employed. In one dimension, such a transformation can be written as

$$I = \int_{-1}^{1} f(x)dx = \int_{-1}^{1} f(a\xi^3 + b\xi^2 + c\xi + d)J(\xi)d\xi, \tag{11}$$

where

$$J = 3a\xi^2 + 2b\xi + c, \tag{12}$$

$$a = (1 - \bar{r})/(1 + 3\bar{\xi}^2), \tag{13}$$

$$b = -3(1 - \bar{r})\bar{\xi}/(1 + 3\bar{\xi}^2), \tag{14}$$

$$c = (\bar{r} + 3\bar{\xi}^2)/(1 + 3\bar{\xi}^2), \tag{15}$$

$$d = -b, \tag{16}$$

where f is the function to be integrated, i.e., Green's function times the shape function in our case. $\bar{\xi}$ is the parametric coordinate of the projected collocation node. $\bar{r}$ is a free parameter which can be taken as a function of the normal distance from the current node to the element. In the two-dimensional case, the transformation in Eq. (11) is applied to both directions (ξ and η).

The key of this transformation is to self-adjust the distribution of integration points. As shown in Fig. 2, the red dots represent the collocation nodes whose velocities are to be calculated, such as nodes on the bilayer. The black dots represent the integration points within an element. The Green's functions of Eqs. (4) and (5) go to infinity when the red dots approach the element, which causes inaccurate calculation of the boundary integral equations using regular integration algorithms, such as the regular Gaussian quadrature. Figure 2(a) illustrates the integration point distribution for the regular Gaussian quadrature. Figure 2(b) illustrates the integration point distribution for this self-adaptive quadrature. Compared with the regular Gaussian quadrature, where integration points are distributed uniformly no matter where the collocation node is located, this transformation leads to the lumping of integration points around the collocation nodes, which significantly enhances the computation accuracy without increasing integration points.

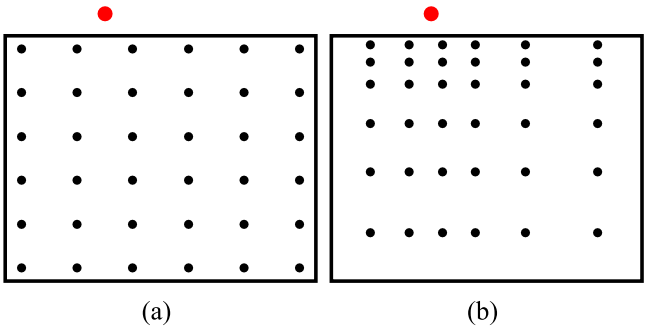

FIG. 2. Distributions of integration points in a quadrilateral element. (a) Regular Gaussian quadrature. (b) Self-adaptive Gaussian quadrature. The red dot represents the collocation node where the velocity is evaluated, such as a node on the RBC bilayer or $\mathbf{x}_0$ in Eq. (8). The black dots represent the integration points. The black quadrilateral represents the element to integrate.

If $\bar{r} = 0$, Eq. (11) degenerates into the coordinate transformation for a singular integral, which is the case when the red dot locates precisely on the element, e.g., a node of the element. In boundary integral equations, the single-layer potential kernel has a weak singularity of $1/r$ ($r = |\mathbf{x} - \mathbf{x}_0|$) as shown in Eq. (4), while the double-layer potential kernel has a singularity of $1/r^2$ ($r = |\mathbf{x} - \mathbf{x}_0|$) as shown in Eq. (5). These singularities can be accurately evaluated by this self-adaptive quadrature.[46] Although it is well known that special quadratures are required to calculate nearly singular integrals,[10,47] they are usually used in high-order spectral representations. But this self-adaptive quadrature can accurately work for our low-order bilinear quadrilateral elements and can work seamless with bilinear shell elements in finite elements. We will demonstrate its accuracy in Sec. VI B.

Another advantage of this algorithm is that it works for all three cases: (1) the red dot is within the element (singular integral); (2) the red dot is away from the element, but its projection point is within the element (nearly singular integral); (3) the red dot is away from the element, and its projection point is outside the element, but it is still within the cut-off distance (nearly singular integral). This not only simplifies the numerical implementation but also ensures the smoothness of the solution when the red dot moves across element edges.

B. Cell-wall interaction

Besides the singular and nearly singular integrals discussed above, we also applied an interaction force between the cell and the wall to capture the repulsive force due to the steric effect of the glycocalyx layer on the RBC surface and associated electrostatic interactions. The thickness of the glycocalyx layer on RBCs is measured as 5–10 nm,[48,49] and it is much thicker on endothelial cells.[50] The glycocalyx layers are negatively charged due to its anionic oligosaccharides, and the typical polydimethylsiloxane (PDMS) surfaces of the microfluidic channel walls used in the experiments are slightly negatively charged as well. It was estimated that this repulsive force would rise significantly when the cell-wall distance h is smaller than 35 nm.[32] We applied a harmonic repulsive force between the cell node and the wall surface. We studied the effect of h by varying it from 35 nm to 100 nm and found that

its influence on our results is small as long as it is within this range. This is not a numerical ad-hoc algorithm, as the extra physics must be taken into account to describe the interactions at the small length scale between the cell and the wall besides hydrodynamic interactions.

In addition, the corner singularities in the computation domain can cause significant error in boundary integral simulations.[51] The Green's functions of Eqs. (4) and (5) diverge at sharp corners, which leads to inaccurate calculation of boundary integral equations. Following Pozrikidis' approach,[51] we enhanced the spatial resolution via mesh optimization in the vicinity of the corners. The size of the elements increases in a geometric fashion with respect to their distances to a corner. The details and verifications about corner singularities are described in Appendix C.

V. MULTISCALE MODEL OF THE RED BLOOD CELL MEMBRANE

The mechanical responses of a RBC membrane involve mechanics at different length scales, ranging from dynamics in the whole cell level (in the micron meter scale) down to the local dynamics of the spectrin and its tension-induced structural remodeling such as domain unfolding and dissociations of spectrins in the protein level (in the nanometer scale). To capture these phenomena together, we developed a multiscale approach including three models at different length scales and connect them by a sequential information-passing multiscale algorithm.[11,52]

The detailed aspects of the three-level multiscale models and their information-passing approach are described in Appendix B. As the current study focuses on the boundary integral formulation, we used the default parameters for our multiscale model as we used in our previous studies,[18,53] which are listed in Tables IV and V in Appendix B, unless specified. The differences between our three-level multiscale RBC model and existing RBC models are summarized in Table II.

This multiscale RBC model has been verified in previous work against various quasi-static and dynamic experiments,[52,53] such as cell stretching by optical tweezer, micropipette aspiration, and RBC deformation in shear flows and tube flows. To couple the boundary integral simulation with the finite element simulation in the Level III model to evaluate the fluid-structure interaction, we used the same bilinear quadrilateral surface mesh for the boundary integral simulation and the finite element simulation (bilinear quadrilateral continuum-based shell elements[54]) of the lipid bilayer. The traction calculated from the finite element simulation is passed to the boundary integral simulation, and the velocity calculated from the boundary integral simulation is used in the finite element simulation to advance the positions of the bilayer nodes using the explicit Euler integration in time.[54] This staggered coupling was verified in previous work by studying motions of RBCs in shear flows and tube flows,[11,18,53,55] such as tumbling, tank-treading, and swinging motions of RBCs in ektacytometry.[56,57] In addition, we used independent meshes for the walls and inlet/outlet in the boundary integral formulation, which are fixed spatially.

VI. VERIFICATION OF NUMERICAL ISSUES AND VALIDATION OF THE COUPLED FINITE ELEMENT AND BOUNDARY INTEGRAL SIMULATIONS

We will first verify our boundary integral formulation step by step to make sure that (1) the Neumann boundary conditions are enforced appropriately and (2) the effects of singular and nearly singular integrals related to strong lubrication interactions are accurately captured. Then we will validate the fluid-structure interaction simulation against the experiment of a RBC squeezing through a submicron slit in a microfluidic device.[26]

A. Verification of the boundary integral formulation with prescribed pressure

To verify our boundary integral formulation with prescribed inlet and outlet pressures, we applied it to solve a Poiseuille flow. The computational domain is a cylindrical tube with a circular cross section. The length of the tube is 30 μm, and the radius of the cross section is 6 μm. On the inlet, a constant pressure of 150 Pa is applied, and the pressure on the outlet is set to be zero. Figure 3 shows the velocity profile.

TABLE II. Comparison of RBC membrane models. WLC: worm-like chain. CGMD: coarse-grained molecular dynamics.

RBC membrane models	Main characteristics	Advantages and disadvantages
Current three-level model (Refs. 52, 11, and 58)	Spanning from spectrin domains, 3D junctional complexes to the whole cell	Molecular-detailed, fast due to sequential passing of pre-calculated information
Empirical constitutive laws (Refs. 59, 60, etc.)	Based on classical thermodynamics and deformation invariants	No molecular details, analytical solutions available (e.g., micropipette), simple, fast
WLC network (Refs. 21, 61, 62, 17, 18, 63, etc.)	Microstructures of the network, WLC model for spectrins but no domain details (the initial shear and area moduli of WLC networks were derived in Ref. 61)	Whole-cell model with individual spectrins modeled, expensive if a full model is used without coarse-graining
CGMD model (Refs. 64, 65, 66, 67, etc.)	Spectrin domains as beads, one-particle-thick bilayer model	Spectrin dissociation, bilayer budding, expensive
Low-order models (Ref. 68)	Coarse-graining, 10 beads per cell	Low-resolution, very fast

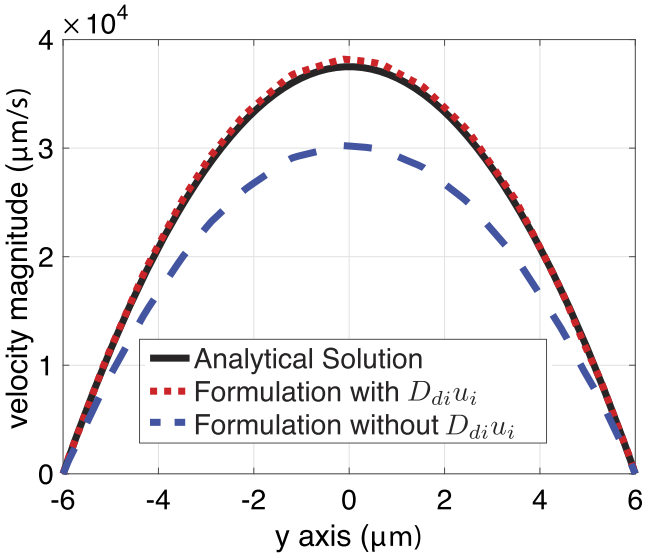

FIG. 3. Verification by the predicted velocity profile of a Poiseuille flow. $D_{di}u_i$ is the contribution from the double-layer potential on the inlet/outlet in Eq. (A19).

The black curve is the analytical solution, and the red curve obtained from our simulation agrees well with the analytical solution.

To estimate the contribution from the velocity distribution on the inlet/outlet, we removed the double-layer potential on the inlet/outlet, i.e., the last term $\frac{1}{8\pi}\int_{\Gamma^N} u_i(\mathbf{x})T_{ijk}(\mathbf{x},\mathbf{x}_0)n_k(\mathbf{x})d\Gamma(\mathbf{x})$ in Eq. (3) or its matrix form of $D_{di}u_i$ in Eq. (A19). The corresponding result is given in Fig. 3 by the blue curve, which shows that this term can contribute more than 20% to the total velocity.

B. Verification of nearly singular integrals

To illustrate the influence of nearly singular integrals, we applied our numerical method to solve the velocity field induced by the squeezing motion of two rigid spheres in a viscous fluid at rest at infinity.[9,69] The two spheres have the same radius of 3 μm. The gap between them is 0.1 μm. We choose a Cartesian coordinate system in which the centers of the two spheres are (0, 3.05, 0) and (0, −3.05, 0), respectively. One sphere is stationary, and the other one is approaching to it with a constant velocity of −10 μm/s parallel to their line of centers.

An asymptotic analytical solution of the flow velocity[9,69] is available for this problem. Since the flow is axisymmetric, the velocity can be given in a cylindrical coordinate system as

$$\begin{aligned} v_r &= \mathrm{U}\frac{1}{r}\frac{\partial\psi}{\partial z}, \\ v_z &= -\mathrm{U}\frac{1}{r}\frac{\partial\psi}{\partial r}, \\ v_\theta &= 0, \end{aligned} \tag{17}$$

where U is the constant velocity of the moving sphere, which is −10 μm/s here. ψ is the Stokes stream function, and its asymptotic form is

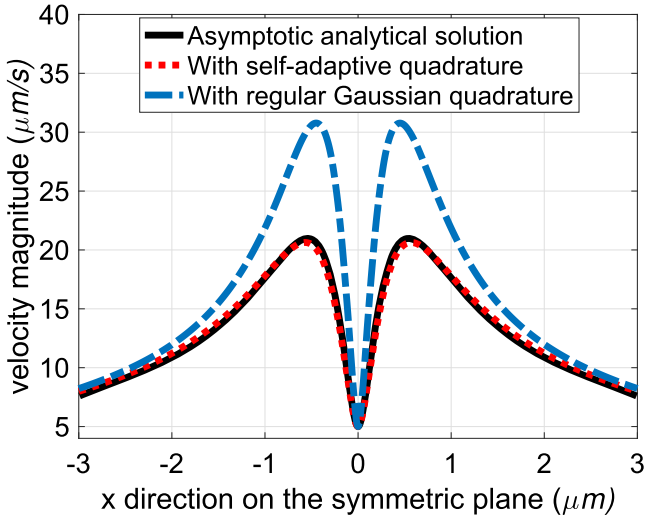

FIG. 4. Velocity in the x direction (y = 0) on the symmetric plane between two spheres.

$$\psi(r,z) = a^2\epsilon\left[\psi_0(r,z) + \epsilon\psi_1(r,z) + \epsilon^2\psi_2(r,z)\right] + \mathrm{O}(\epsilon^4), \tag{18}$$

where a is the radius of the two spheres, namely, 3 μm here. ϵ is the ratio of the gap width to the sphere radius. The detailed expressions of ψ_0, ψ_1, and ψ_2 are given in Jeffrey's paper[69] and Kim and Karrila's book.[9]

In Fig. 4, we plotted the velocity profile in the x direction (y = 0) on a symmetric plane. The black curve is the asymptotic analytical solution from Eq. (17). The red curve is obtained by evaluating the boundary integral equations using the self-adaptive quadrature discussed in Sec. IV A. By contrast, the blue curve is the result using the regular Gaussian quadrature. It can be clearly seen that the self-adaptive quadrature accurately captures the strong hydrodynamic interaction between the two spheres, while the regular Gaussian quadrature performs much worse due to the inaccurate calculation of the nearly singular integrals.

C. Validation of cell deformation against experiments

To validate our coupled numerical methods including the boundary integral method, the multiscale RBC model, and their fluid-structure interaction, we simulated the process of a RBC squeezing through a submicron slit and compared the cell deformations with a submicron slit experiment carried out by our collaborator Gambhire *et al.*[70] (see Acknowledgments). As noted in Sec. V, the multiscale RBC model has been validated against various quasi-static and dynamic experiments.[52,53] Snapshots of the cell deformations at different time steps during the passage in the experiment and our simulation are shown in Figs. 5(a) and 5(b), respectively. The computational domain in our simulation is built based on the geometry of the microfluidic device used in the experiment. According

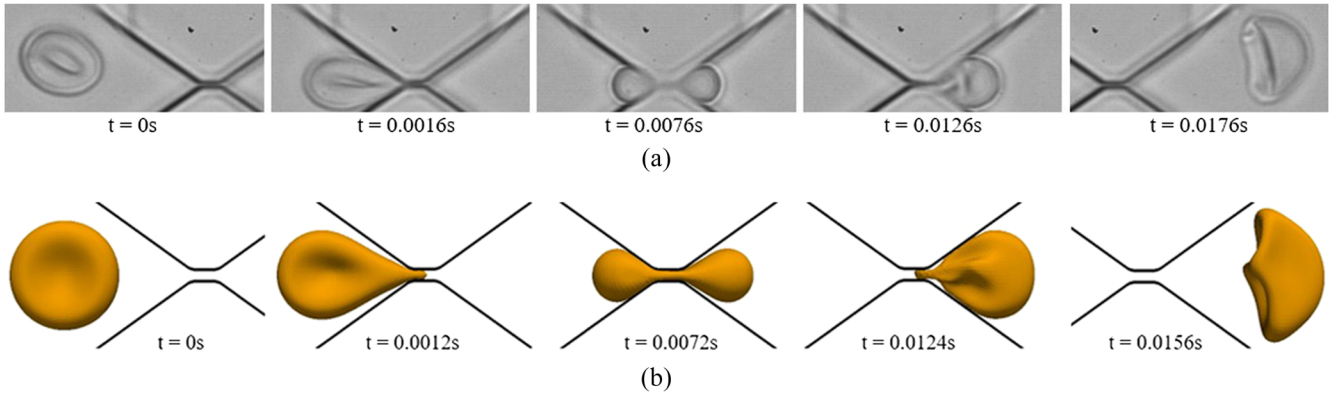

FIG. 5. Validation by simulating the submicron slit experiments on healthy RBCs. The length of this artificial slit is 1.93 μm, the width is 0.84 μm, and the depth is 5.0 μm. The pressure drop is 831 Pa in both the experiment and our simulation. (a) Cell deformations in the experiment at time steps t = 0 s, t = 0.0016 s, t = 0.0076 s, t = 0.0126 s, and t = 0.0176 s [courtesy of Anne Charrier, Annie Viallat, and Emmanuele Helfer (see Ref. 70)]. (b) Cell deformations in the numerical simulation at time steps t = 0 s, t = 0.0012 s, t = 0.0072 s, t = 0.0124 s, and t = 0.0156 s.

to the experimental measurements, the length of this artificial slit is 1.93 μm, the width is 0.84 μm, and the depth is 5.0 μm.[26] It is very close to the dimensions of inter-endothelial slits in the human spleen.[38] The boundary conditions in our simulation are consistent with the experiment. The pressure drop between the inlet and outlet is 831 Pa. The viscosity ratio between the fluids inside and outside the cell membrane is 5.0. By comparing Figs. 5(a) and 5(b), we can clearly see that the cell deformations at different time steps in our simulation resemble those in the experiment. To the best of our knowledge, this is the first experimental validation of numerical simulations related to splenic filtration of RBCs, while no experimental validation has been done in the existing computational studies.[25,27,30–32,36]

For simulations conducted in this study, 3052 four-node quadrilateral elements with 3054 nodes are used to discretize the lipid bilayer, 2551 four-node quadrilateral elements with 2595 nodes are used to discretize the channel wall, and 224 four-node quadrilateral elements with 270 nodes are used to discretize the inlet and outlet. The code is parallelized using Message Passing Interface (MPI). It took 16 h to run using 8 cores of Intel Xeon E5-2680 v3 at 2.50 GHz CPUs with the viscosity ratio of 5.0. For the cases with equal viscosities, the computational time is reduced by several folds. The same numbers of elements are used in the following parametric study simulations. Table III is a summary of the computational costs for the boundary integral simulation and the finite element simulation. The most expensive part is the iterations for $\lambda \neq 1$ in the boundary integral simulations.

TABLE III. Relative computational cost at different viscosity ratios with 8 core MPI parallelization.

Viscosity ratio	FEM time (%)	BEM time (%)	Number of iterations
1.0	34	66	1
3.0	26	74	5-11
5.0	17	83	9-20

VII. RESULT

After the above verifications and validations, we carried out parametric studies of RBCs passing through submicron slits. We examined the transit time, bilayer tension, cytoskeleton shear deformation, and bilayer-cytoskeletal interaction stress among various outputs. The transit time t_T is defined as $t_T = t_2 - t_1$, where t_1 is the time when any node of the cell mesh first enters the slit and t_2 is the time when the cell completely leaves the slit. The prolonged transit time of a RBC may significantly increase the chance of its capture by macrophages. The bilayer tension is an important measurement which determines the opening of the mechanosensitive channels such as PIEZO1[71,72] in RBCs and the bilayer rupture.[73] The cytoskeletal deformation is measured by the maximum shear ratio λ_1/λ_2, where λ_1 and λ_2 are the principal stretches which define the in-plane deformation. The cytoskeletal deformation can be used to evaluate whether spectrin unfolding and spectrin dimer dissociation may occur.[58] The bilayer-cytoskeletal interaction force plays a major role in bilayer-cytoskeletal detachment, leading to bilayer budding and surface area loss, which is critical in hereditary spherocytosis (HS), hereditary elliptocytosis (HE), and RBC aging.[18]

We used a standard case with a pressure drop of 400 Pa, cell volume of 93.88 μm^3, cell surface area of 146.56 μm^2, viscosity ratio of 1.0, and initial cytoskeleton shear modulus of 7.5 pN/μm. Then we studied the effects of the pressure drop, volume-to-surface ratio, viscosity ratio, and initial cytoskeleton shear modulus.

A. Effect of pressure drop

We studied five cases with pressure drops of 100 Pa, 200 Pa, 400 Pa, 600 Pa, and 800 Pa. The pressure drop across individual slits was estimated between 150 Pa and 1000 Pa in the existing experiments for the slits with a depth of 5 μm.[26] Figure 6(a) shows the maximum shear ratio λ_1/λ_2 and the transit time under different pressure drops. Figure 6(b) shows the maximum bilayer tension and the maximum

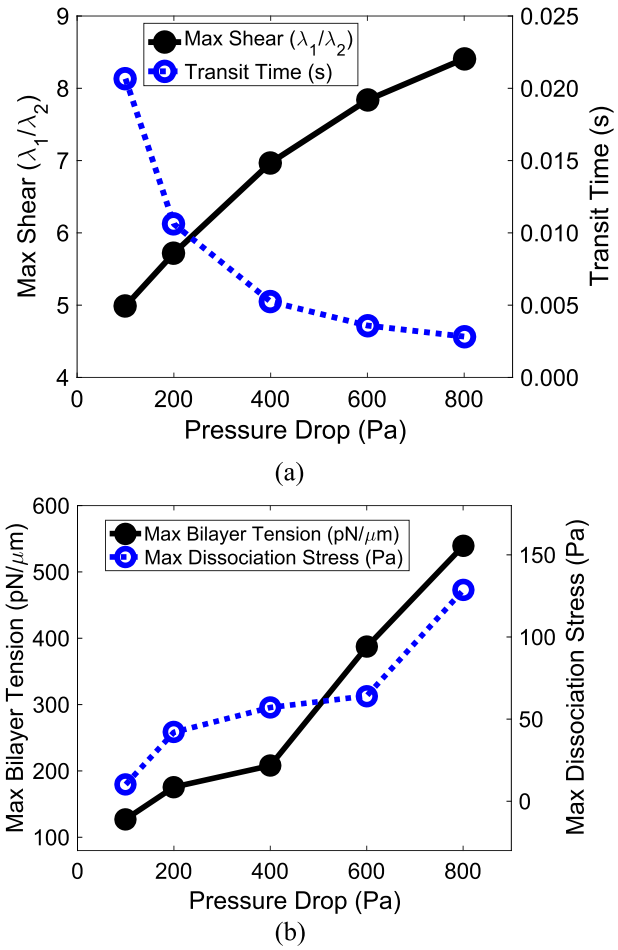

FIG. 6. Effect of the pressure drop. (a) The maximum cytoskeleton shear deformation and transit time. (b) The maximum bilayer tension and the maximum bilayer-cytoskeletal dissociation stress.

bilayer-cytoskeletal dissociation stress. Higher pressure drop causes higher velocity and stress in the slit, which leads to larger cell deformation. When the pressure drop is increased from 100 Pa to 800 Pa, the maximum shear ratio λ_1/λ_2 increases rapidly from 5.0 to 8.5 so that the spectrin could be stretched by more than 2.5 times under high hydrodynamic pressure. The cell also passes through the slit much faster. When the pressure drop is 800 Pa, it only takes one fifth of the time for the cell to pass through compared with the pressure drop of 100 Pa. It means that the chance for the cell to get trapped in the slit is much higher when the pressure drop is below 100 Pa. The maximum bilayer tension increases with increased pressure drop. It reaches 550 pN/μm under the pressure drop of 800 Pa. It could be large enough to open the mechanosensitive channels and may further change the cell volume, as the critical tension for opening the mechanosensitive channels is estimated as 680 pN/μm.[72] But it is still too small to rupture the bilayer, as the bilayer lysis tension is estimated as 10 000 pN/μm.[73] On the other hand, the change of bilayer tension is relatively small when the pressure drop varies from 200 Pa to 400 Pa. We examined this in detail and found that at 200 Pa, the maximum tension happens during the exit of the slit, but for pressure drops of 100 Pa and 400 Pa, the maximum tension occurs when the cell is inside the slit. The bilayer-cytoskeletal dissociation stress increases at higher pressure and reaches 150 Pa when the pressure drop is 800 Pa, which is still smaller than the critical stress to break the bilayer-cytoskeletal bonds (>1000 Pa[32]).

B. Effect of volume-to-surface ratio

We studied five cases with cell surface areas of 125.368 μm^2, 129.077 μm^2, 133.903 μm^2, 139.758 μm^2, and 143.048 μm^2. We kept the cell volume as a constant of 93.880 μm^3 and changed the cell shape by scaling the x and y directions by a factor of s and scaling the z direction by a factor of $1/s^2$. The maximum shear ratio λ_1/λ_2 and the transit time

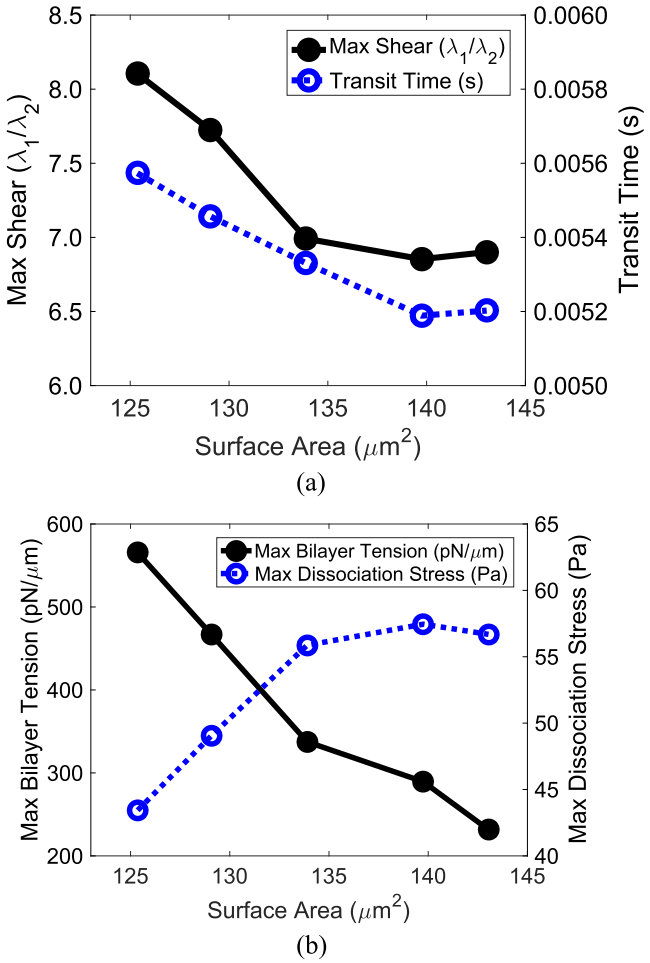

FIG. 7. Effect of the volume-to-surface-area ratio. The volume is kept as a constant of 93.88 μm^3 while the surface area is varied. (a) The maximum cytoskeleton shear deformation and transit time. (b) The maximum bilayer tension and the maximum bilayer-cytoskeletal dissociation stress.

are shown in Fig. 7(a). The maximum bilayer tension and the maximum bilayer-cytoskeletal dissociation stress are shown in Fig. 7(b). The transit time decreases when the cell surface area is increased, which is consistent with the experimental and clinical observations. When RBCs lose the surface area such as aged RBCs and HS/HE RBCs, it may take longer time for them to pass through the splenic slit, leading to a higher chance of clearance by macrophages. Both the shear deformation and bilayer tension decrease when the cell surface area is increased. The maximum bilayer tension of RBCs with a small surface area of 125 μm^2 is close to 600 pN/μm, which may also cause the mechanosensitive channels to open. The maximum bilayer-cytoskeletal dissociation stress increases with increased surface area, but the dissociation stress shown here is still too small to break the bilayer-cytoskeletal bonds.[32]

C. Effect of the viscosity ratio

We explored the effect of the viscosity ratio between the fluids inside and outside the cell membrane. The viscosity ratios are chosen to be 0.75, 1.0, 2.0, 3.5, and 5.0. The maximum shear ratio λ_1/λ_2 and the transit time are illustrated in Fig. 8(a). The maximum bilayer tension and the maximum bilayer-cytoskeletal dissociation stress are shown in Fig. 8(b). We found that the effect of the viscosity ratio on shear deformation and bilayer-cytoskeletal dissociation stress is relatively small. On the other hand, the transit time increases linearly with the increased viscosity ratio. For sickled RBCs, whose viscosity is much higher than healthy RBCs, it may take a longer time for them to pass through the inter-endothelial slits and increase the chance of their capture by macrophages. The maximum bilayer tension increases with a higher viscosity ratio, but less than 500 pN/μm. Overall, the effect of

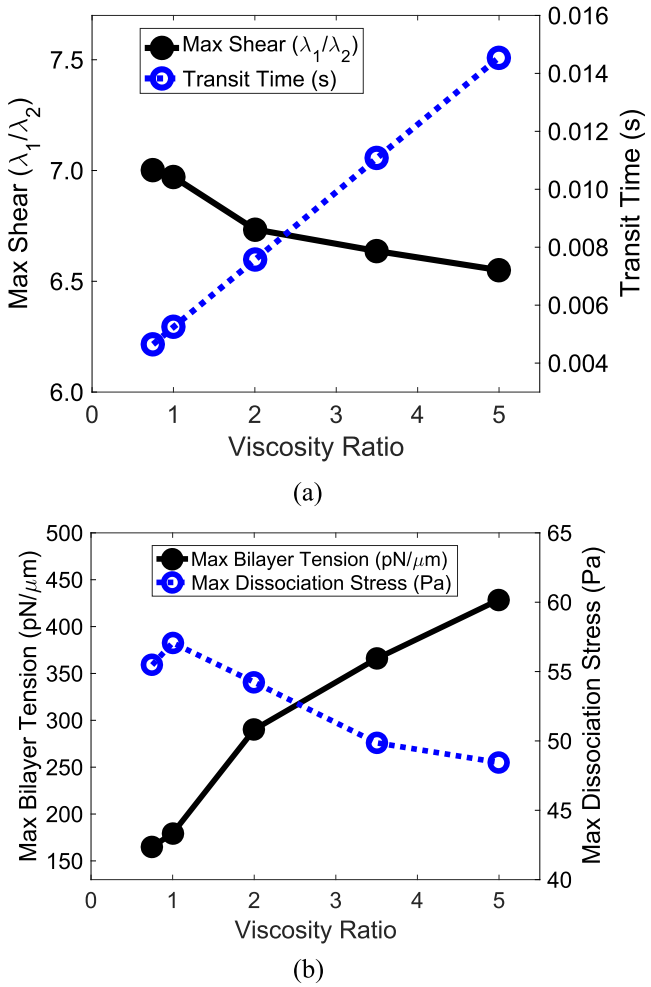

FIG. 8. Effect of the viscosity ratio. (a) The maximum cytoskeleton shear deformation and transit time. (b) The maximum bilayer tension and the maximum bilayer-cytoskeletal dissociation stress.

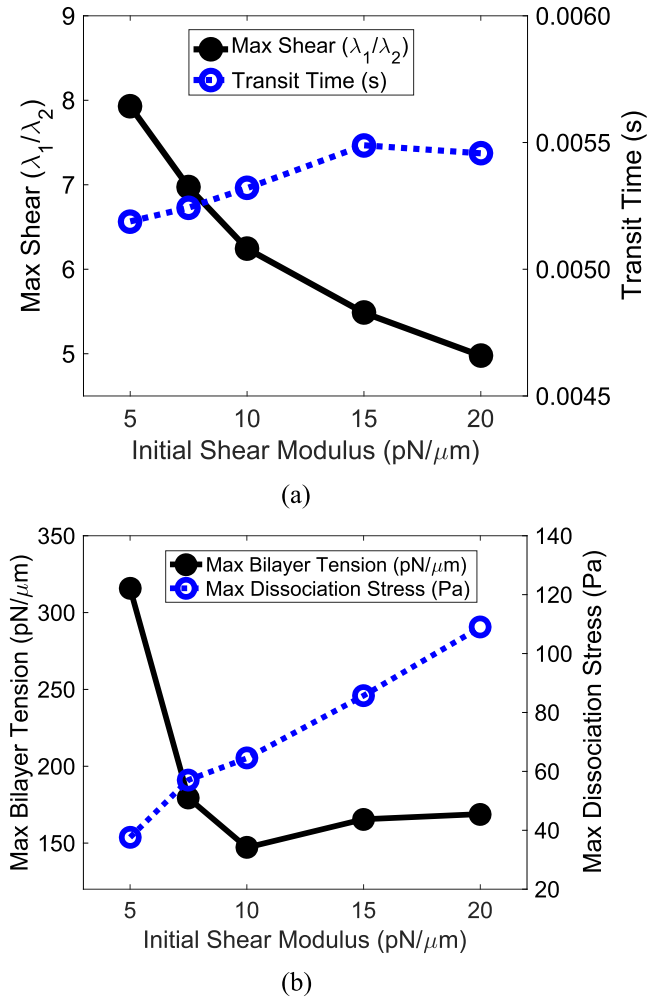

FIG. 9. Effect of initial cytoskeleton shear modulus. (a) The maximum cytoskeleton shear deformation and transit time. (b) The maximum bilayer tension and the maximum bilayer-cytoskeletal dissociation stress.

the viscosity ratio is more important for the bilayer than the cytoskeleton.

D. Effect of cytoskeleton shear modulus

We studied five cases with initial cytoskeleton shear modulus of 5.0 pN/μm, 7.5 pN/μm, 10.0 pN/μm, 15.0 pN/μm, and 20.0 pN/μm. It was found that the shear modulus of RBCs is increased by one order in malaria-infected RBCs or in Southeast Asian Ovalocytosis (SAO).[74,75] The study of the effect of cytoskeleton shear modulus could help us understand the special behaviors of these diseased RBCs when they pass through the splenic slits. We adjusted the persistence length of the spectrin in our multiscale RBC model to get these different initial shear moduli for a parametric study. Figure 9(a) shows the maximum shear ratio λ_1/λ_2 and the transit time. Figure 9(b) shows the maximum bilayer tension and the maximum bilayer-cytoskeletal dissociation stress. The transit time increases slightly with larger initial shear modulus, and the cytoskeleton shear modulus may have a non-significant impact on the retention rate of RBCs in the slit. The bilayer tension first reduces rapidly and then becomes constant when the cytoskeleton shear modulus is increased. Its maximum value is only about 300 pN/μm. When the initial cytoskeleton shear modulus is increased, the maximum shear ratio decreases quickly while the maximum bilayer-cytoskeletal dissociation stress increases rapidly. In brief, the increased cytoskeleton shear modulus enhances the mechanical role of the cytoskeleton compared to the bilayer in this composite membrane.

Putting together the effects of the viscosity ratio and the shear modulus, our results show that the increased viscosity ratio enhances the role of the bilayer and reduces the role of the cytoskeleton in the composite membrane, while increased shear modulus has the opposite effect by increasing the role of the cytoskeleton and downplaying the role of the bilayer.

E. Temporal and spatial distributions of cytoskeletal shear deformation, bilayer tension, and bilayer-cytoskeletal interaction in a RBC

We examined the spatial distributions of cytoskeletal shear deformation, bilayer tension, and bilayer-cytoskeletal interaction stress at different time steps when a RBC is passing through the slit. The distributions of shear ratio λ_1/λ_2 in the cytoskeleton are shown in Fig. 10. Before the cell enters the slit, the shear ratio over the cell membrane is very close to 1.0. Only for a small part which already gets inside the slit, the shear ratio is higher than 1.0. When the cell is squeezing through the slit, the shear ratio of the membrane inside the slit increases rapidly. With a diameter of about 8.0 μm, the cell has to undergo large deformation to pass through the slit with a width of 0.84 μm, which causes the significant cytoskeletal shear deformation. After the cell exits the slit completely, the shear ratio reduces to 1.0 with the recovery of cell shape.

The distributions of the bilayer tension and bilayer-cytoskeletal interaction stress at different time steps are shown in Figs. 11 and 12, respectively. Similarly, before the cell enters the slit, both the bilayer tension and bilayer-cytoskeletal interaction stress are very small and increase rapidly when the cell is passing through the narrow slit due to large cell deformation. While the maximum bilayer tension is concentrated on the rear part of the cell membrane, the maximum bilayer-cytoskeletal interaction stress is concentrated on the membrane which is right inside the slit with positive values, which means that bilayer and

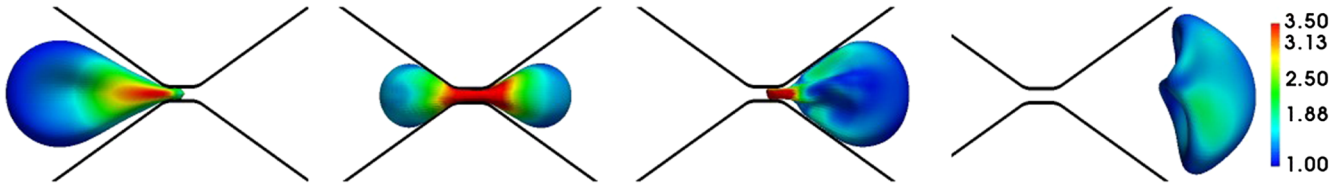

FIG. 10. Temporal snapshots of cytoskeleton shear deformation distributions at time t = 0.0012 s, t = 0.0072 s, t = 0.0124 s, and t = 0.0156 s. The shear deformation is defined as the shear ratio λ_1/λ_2, where λ_1 and λ_2 are the principal stretches.

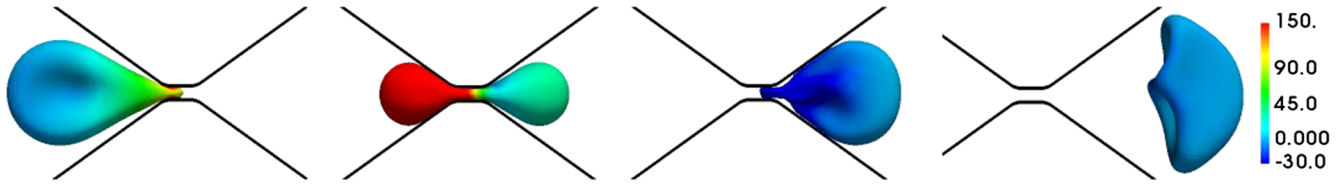

FIG. 11. Temporal snapshots of bilayer tension distributions at time t = 0.0012 s, t = 0.0072 s, t = 0.0124 s, and t = 0.0156 s. Positive values mean tension, while negative values mean compression. Unit: pN/μm.

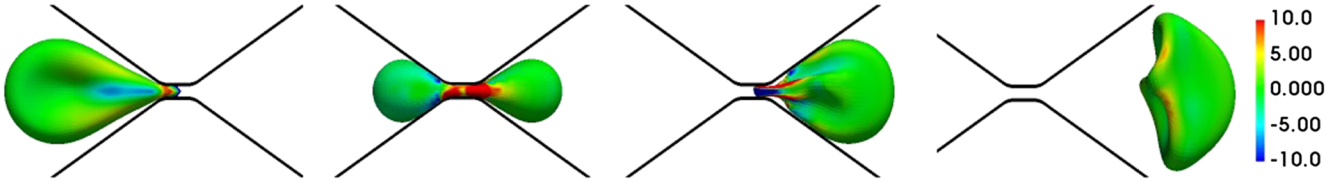

FIG. 12. Temporal snapshots of bilayer-cytoskeletal interaction stress distributions at time t = 0.0012 s, t = 0.0072 s, t = 0.0124 s, and t = 0.0156 s. Positive values mean that the bilayer and the cytoskeleton are associating with each other, while negative values mean that they are dissociating from each other (dissociation stress). Unit: Pa.

cytoskeleton tend to associate together. Just before the cell exits the slit (t = 0.0124 s), the bilayer-cytoskeletal dissociation stress reaches its maximum at the trailing edge, which suggests that the cytoskeleton tends to dissociate from the bilayer. After the cell exits the slit, the cell shape is recovered and the bilayer tension and the bilayer-cytoskeletal interaction stress are reduced quickly.

VIII. CONCLUSIONS AND DISCUSSIONS

The verifications and results show that the formulated boundary integral method with the Neumann boundary condition can successfully and accurately predict the dynamics of a RBC squeezing through a submicron slit. The information such as cell deformation, transit time, and internal stress will shed insights on rich behaviors of RBCs in the microfluidic experiments and the corresponding splenic filtration process. We systematically investigated the effects of pressure drop, volume-to-surface-area ratio, internal viscosity, and membrane stiffness on RBC deformation and internal stress. We found that the spectrin could be stretched by more than 2.5 times under high pressure. We predicted that the bilayer tension could be more than 500 pN/μm, which might open the mechanosensitive channels but cannot rupture the bilayer. We also found that the bilayer-cytoskeletal dissociation stress is too low to induce vesiculation. Furthermore, the bilayer tension, cytoskeleton shear deformation, and bilayer-cytoskeletal dissociation stress obtained from the current model will be further coupled with molecular-detailed models of mechanosensitive channels[72] and the bilayer budding process[66] to explore the physics and mechanisms of diseased RBCs when they pass through the splenic slit, such as sickled RBCs, hereditary spherocytosis (HS) RBCs, and hereditary elliptocytosis (HE) RBCs. We will also further explore the effect of spectrin unfolding on healthy and diseased RBCs passing through the slits under high hydrodynamic pressure.

The boundary integral formulation developed will not only be important for understanding RBCs physiology and diseases related to splenic filtrations but also be useful for studying elastic capsules, vesicles, and other cells squeezing through narrow slits in drug delivery and extravasation. Two examples are (1) cancer cells from a primary tumor pass through inter-endothelial slits in blood vessel walls in order to get into the blood circulation and transmigrate to distant organs; (2) white blood cells adhering to the blood vessel endothelium often squeeze through the inter-endothelial slits to target an infection site.

Furthermore, it was recently found that blood plasma behaves as a Boger fluid,[76,77] having a constant shear viscosity and strain-varying extensional viscosity. In particular, Varchanis *et al.*[77] predicted that strain hardening in human blood plasma starts at about 550/s elongational rate and leads to several orders of magnitude jump in elongational viscosity. From our simulation, we found that the elongation rate in the microfluidic experiment can be more than 4000/s. Although the water solution, a Newtonian fluid, was used in the microfluidic experiments, the large elongation rate indicates that under *in vivo* conditions, the normal stresses exerted on the RBC and the wall might be significantly affected by the presence of long proteins that exist in the lubrication layer of the blood plasma. The cytoplasm of general eukaryotic cells is non-Newtonian,[78,79] while the cytoplasm of RBCs is hemoglobin solution and showed Newtonian behavior in bulk solution,[1] but whether it behaves exactly as a Newtonian fluid within such a narrow submicron slit remains unknown.

ACKNOWLEDGMENTS

We thank Anne Charrier, Annie Viallat, and Emmanuele Helfer from Aix-Marseille Universite in France for providing the images of their microfluidic submicron slit experiments for the validation of our simulations. Z.P. and H.L. acknowledge support from the National Science Foundation (Grant No. 1706436-CBET) and the Indiana Clinical and Translational Sciences Institute (Grant No. UL1TR001108) from the National Institutes of Health, National Center for Advancing Translational Sciences, and Clinical and Translational Sciences Award. Most simulations were conducted at the Notre Dame Center for Research Computing (CRC). Some simulations were conducted in the Extreme Science and Engineering Discovery Environment (XSEDE), which is supported by National Science Foundation Grant No. ACI-1548562, through Allocation No. TG-MCB180016. The authors acknowledge the Texas Advanced Computing Center (TACC) at The University of Texas at Austin for providing HPC resources that have contributed to the research results reported within this paper. The authors have no competing interests to declare.

APPENDIX A: NUMERICAL PROCEDURES TO SOLVE THE COUPLED BOUNDARY INTEGRAL EQUATIONS ON THE BILAYER, THE INLET/OUTLET, AND THE WALL

In this section, we will describe how to solve Eqs. (8)–(10) together for the unknown velocity on the interface, the unknown velocity on the inlet/outlet, and the unknown traction on the wall. Let us apply the following lower indices to denote different boundaries, interface, and domains: w (wall), c (cell/capsules membrane), i (inlet and outlet), and d (domain point). We apply four node bilinear quadrilateral boundary elements with the collocation points on the nodes to discretize the boundary integral equations and write the boundary element discretization equations in matrix and vector forms.

1. In the cases of equal viscosity ($\lambda = 1$)

When the viscosity ratio of fluids inside and outside the cell membrane is 1.0, the double layer potential terms of the bilayer disappear, and the nodal velocity vector on the wall from Eq. (10) becomes

$$u_w = S_{ww}f_w + S_{wi}f_i + S_{wc}f_c + D_{ww}u_w + D_{wi}u_i, \tag{A1}$$

where f_w, f_i, and f_c are the nodal traction vectors on the wall, inlet/outlet and bilayer interface with dimensions of $3N_w$ (N_w is the node number of the wall mesh), $3N_i$ (N_i is the node number of the inlet/outlet mesh), and $3N_c$ (N_c is the node number of the interface mesh). u_w and u_i are the nodal velocity vectors with dimensions of $3N_w$ and $3N_i$, respectively. S_{ww}, S_{wi}, and S_{wc} are the matrices of the single-layer potential terms in Eq. (10). D_{ww} and D_{wi} are the matrices of the double-layer potential terms in Eq. (10).

Following similar notations, the nodal velocity vector on the inlet/outlet from Eq. (9) can be written as

$$u_i = S_{iw}f_w + S_{ii}f_i + S_{ic}f_c + D_{iw}u_w + D_{ii}u_i. \tag{A2}$$

The nodal velocity vector on the bilayer interface from Eq. (8) is

$$u_c = S_{cw}f_w + S_{ci}f_i + S_{cc}f_c + D_{cw}u_w + D_{ci}u_i. \tag{A3}$$

Since the velocity of the wall is given as the Dirichlet boundary condition and the traction on the inlet/outlet is given as the Neumann boundary condition, the unknowns in Eqs. (A1) and (A2) are f_w and u_i. We first rearrange Eq. (A1) and write f_w as

$$f_w = -S_{ww}^{-1}(-u_w + S_{wi}f_i + S_{wc}f_c + D_{ww}u_w + D_{wi}u_i). \tag{A4}$$

Then we substitute Eq. (A4) into Eq. (A2); thus, the only unknown left in Eq. (A2) is u_i and can be solved as

$$\begin{aligned} u_i = {} & (I + S_{iw}S_{ww}^{-1}D_{wi} - D_{ii})^{-1}(-S_{iw}S_{ww}^{-1}) \\ & \times(-u_w + S_{wi}f_i + S_{wc}f_c + D_{ww}u_w) \\ & + (I + S_{iw}S_{ww}^{-1}D_{wi} - D_{ii})^{-1}(S_{ii}f_i + S_{ic}f_c + D_{iw}u_w). \end{aligned} \tag{A5}$$

Finally the cell velocity can be calculated by Eq. (A3) with f_w given by Eq. (A4) and u_i given by Eq. (A5). In addition, the velocity of the points within the fluid domain can be solved by Eq. (3) as

$$u_d = S_{dw}f_w + S_{di}f_i + S_{dc}f_c + D_{dw}u_w + D_{di}u_i. \tag{A6}$$

2. In the cases of non-equal viscosity ($\lambda \neq 1$)

When the viscosity ratio of fluids inside and outside the cell membrane is not 1.0, the nodal velocity vector on the wall should include the double layer potential term of the bilayer

$$u_w = S_{ww}f_w + S_{wi}f_i + S_{wc}f_c + D_{ww}u_w + D_{wi}u_i + D_{wc}u_c. \tag{A7}$$

Similarly, the nodal velocity vector on the inlet/outlet is given as

$$u_i = S_{iw}f_w + S_{ii}f_i + S_{ic}f_c + D_{iw}u_w + D_{ii}u_i + D_{ic}u_c. \tag{A8}$$

The nodal velocity vector on the bilayer interface is

$$u_c = S_{cw}f_w + S_{ci}f_i + S_{cc}f_c + D_{cw}u_w + D_{ci}u_i + D_{cc}u_c. \tag{A9}$$

We applied a successive iteration method[8] to solve Eqs. (A7)–(A9). At each iteration step, u_c, u_i, and f_w can be updated as

$$\begin{aligned} u_c^{n+1} = {} & S_{cw}f_w^{n+1} + S_{ci}f_i + S_{cc}f_c + D_{cw}u_w \\ & + D_{ci}u_i^{n+1} + D_{cc}u_c^n, \end{aligned} \tag{A10}$$

$$u_i^{n+1} = u_i^0 + u_i'(u_c^n), \tag{A11}$$

$$f_w^{n+1} = f_w^0 + f_w'(u_c^n), \tag{A12}$$

where $(\cdot)^0$ indicates values when $\lambda = 1$; thus, u_i^0 and f_w^0 are computed by Eqs. (A5) and (A4), respectively. $u_i'(u_c^n)$ and $f_w'(u_c^n)$ are the extra contributions from u_c^n due to viscosity contrast ($\lambda \neq 1$) and are updated as

$$\begin{aligned} u_i'(u_c^n) = {} & (I + S_{iw}S_{ww}^{-1}D_{wi} - D_{ii})^{-1} \\ & \times(D_{ic}u_c^n - S_{iw}S_{ww}^{-1}D_{wc}u_c^n), \end{aligned} \tag{A13}$$

$$f_w'(u_c^n) = -S_{ww}^{-1}(D_{wi}u_i'(u_c^n) + D_{wc}u_c^n). \tag{A14}$$

Based on Eq. (A3), we can rewrite Eq. (A10) as

$$u_c^{n+1} = u_c^0 + S_{cw}f_w'(u_c^n) + D_{ci}u_i'(u_c^n) + D_{cc}u_c^n, \tag{A15}$$

where u_c^0 is the bilayer velocity when $\lambda = 1$ and is calculated by Eq. (A3).

We will obtain $u_c^{n+1} \approx u_c^n$ after Eqs. (A7)–(A9) are solved using the above successive iteration method.[8] Since the initial velocity for the first iteration step is obtained from the previous time step in the motion of the capsule, which is close to the current velocity, the iteration number is usually less than 20.

Furthermore, the velocity of the points within the fluid domain can be solved as

$$u_d = S_{dw}f_w + S_{di}f_i + S_{dc}f_c + D_{dw}u_w + D_{di}u_i + D_{dc}u_c. \quad \text{(A16)}$$

3. In the cases without a cell/capsule

The traction f_c and velocity u_c on the interface disappear, so the nodal velocity vector on the inlet/outlet becomes

$$\begin{aligned} u_i = {} & (I + S_{iw}S_{ww}^{-1}D_{wi} - D_{ii})^{-1} \\ & \times \left\{-S_{iw}S_{ww}^{-1}(-u_w + S_{wi}f_i + D_{ww}u_w)\right\} \\ & + (I + S_{iw}S_{ww}^{-1}D_{wi} - D_{ii})^{-1}(S_{ii}f_i + D_{iw}u_w). \end{aligned} \quad \text{(A17)}$$

The nodal traction vector on the wall is

$$f_w = -S_{ww}^{-1}(-u_w + S_{wi}f_i + D_{ww}u_w + D_{wi}u_i), \quad \text{(A18)}$$

and the velocity of the points within the fluid domain is

$$u_d = S_{dw}f_w + S_{di}f_i + D_{dw}u_w + D_{di}u_i. \quad \text{(A19)}$$

APPENDIX B: MULTISCALE MODEL OF RBC MEMBRANES

As illustrated in Fig. 13, the three-level multiscale models and the sequential information-passing approach to connect them together are described as follows.

1. A modified entropic spring model of spectrin (Sp) with domain unfolding (Level I)

Spectrin is the major structural protein that determines the constitutive behavior of the RBC cytoskeleton.

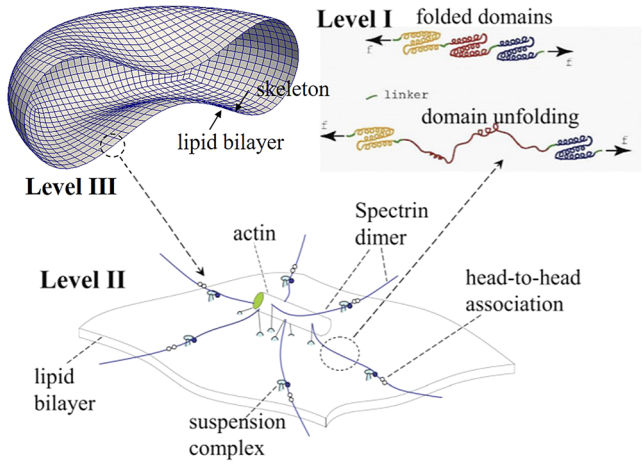

FIG. 13. Three-level multiscale model of a red blood cell. Level I, spectrin (Sp) constitutive model; Level II, junctional complex (JC) model; Level III, whole-cell model.

TABLE IV. Bilayer parameters: h_b is the effective bilayer thickness, μ_b is the shear modulus, K_b is the area modulus, and k_c is the bending stiffness.

h_b (nm)	μ_b (pN/μm)	K_b (pN/μm)	k_c(J)
2.2	10^{-3}	5×10^5	2×10^{-19}

TABLE V. Cytoskeletal parameters: L_f and L_u are the contour lengths of the folded and unfolded domains, p_f and p_u are the persistence lengths of folded and unfolded domains, $\Delta\Delta x^* = \Delta x_{f\to u} - \Delta x_{u\to f}$ is the difference between the activation lengths of the unfolding and refolding processes, and $F_{1/2}$ is the force by which half of the domains are unfolded.

p_f (nm)	p_u (nm)	L_f (nm)	L_u (nm)	$\Delta\Delta x^*$ (nm)	$F_{1/2}$ (pN)
8.41	0.8	6.39	39	12.6	12

As a highly flexible biopolymer, it is usually modeled by the worm-like chain (WLC) depiction.[21,62] This depiction, however, does not take into account the fact that spectrins can be overstretched, i.e., it can be stretched beyond its original contour length due to the existence of multiple domains that unfold under sufficient loading. Without proper representation of this process of domain unfolding, the cytoskeletal stiffness might be overestimated during large deformations. Towards this end, we have developed a modified entropic spring model of Sp by representing its folding/unfolding reactions as thermally activated processes.[52,58] The force-length curve $F = F(x, \dot{x})$ of a spectrin monomer can be determined by the following equations:

$$\frac{x}{NL_f} = (1-\phi_u)\mathcal{L}\left(\frac{2Fp_f}{k_BT}\right) + \phi_u\mathcal{L}\left(\frac{2Fp_u}{k_BT}\right)\frac{L_u}{L_f}, \quad \text{(B1)}$$

$$\phi_u = \frac{\exp\left(\frac{(F-F_{1/2})\Delta\Delta x^*}{k_BT}\right)}{1+\exp\left(\frac{(F-F_{1/2})\Delta\Delta x^*}{k_BT}\right)} \quad \text{if } \dot{x} \approx 0, \quad \text{(B2)}$$

where x is the length of the spectrin monomer, $N = 19$ is the total number of domains in a spectrin monomer, L_f and L_u are the contour lengths of the folded and unfolded domains, ϕ_u is the fraction of unfolded domains, $\mathcal{L}(\zeta) = \coth\zeta - 1/\zeta$ is the Langevin function, p_f and p_u are the persistence lengths of folded and unfolded domains, $\Delta\Delta x^* = \Delta x_{f\to u} - \Delta x_{u\to f}$ is the difference between the activation lengths of the unfolding and refolding processes, and $F_{1/2}$ is the force by which half of the domains are unfolded. The values of these parameters are shown in Table V. In general, the force $F(x, \dot{x})$ depends on the stretching rate as well and ϕ_u is calculated via Monte Carlos simulations.[58] Under the quasi-static assumption when the stretching is very slow, ϕ_u is given by Eq. (B2). k_B is the Boltzmann constant, and $T = 310$ K is the temperature.

2. A molecular-based model of junctional complex (JC) (Level II)

Consisting of a central piece of short actin protofilament connected with up to six Sp. The junctional complex (JC) is the basic repeating unit in the cytoskeleton of an erythrocyte, as shown in Fig. 13 (Level II). A molecular-based model that incorporates the state-of-the-art understanding of the exact molecular architecture of a JC (including, e.g., the exact configuration of actin-spectrin connectivity) has been developed.[52,58] The mean stress resultant τ_a and the shear modulus μ can be calculated from this JC model by evaluating the derivatives of the free energy density w of the system with respect to the deformation invariants α and β,

$$\tau_a(\alpha,\beta) = \frac{\partial w(\alpha,\beta,\mathrm{F})}{\partial \alpha}, \quad \mu(\alpha,\beta) = \frac{\partial w(\alpha,\beta,\mathrm{F})}{\partial \beta}, \tag{B3}$$

where F is the force-length curve of the spectrin monomer obtained from Eq. (B1) in the Level I model and w is the free energy density. These properties of the cytoskeleton (τ_a, μ) are predicted as tabulated two-variable functions of deformation in terms of area invariants $\alpha = \lambda_1\lambda_2 - 1$ and shear invariant $\beta = (\lambda_1^2 + \lambda_2^2)/(2\lambda_1\lambda_2) - 1$ defined by Evans and Skalak,[60] and they are passed to calculate stresses at the integration points of shell elements in the Level III whole-cell model. λ_1 and λ_2 are the principal stretches and can be calculated from the polar decomposition of the deformation gradient $\mathbf{G}$.

3. A whole-cell model (Level III)

A key structural feature of the RBC is the mobile connectivity between its lipid bilayer and cytoskeleton. This is caused by the fact that these two components are connected through pinning points made of transmembrane proteins, which can drift within the fluid-like lipid bilayer. In the Level III model, we depict the cell membrane as two separate layers. The outer layer corresponds to the lipid bilayer, which has large area stiffness, negligible shear stiffness, and finite bending stiffness. The inner layer, with finite area and shear moduli, represents the cytoskeleton. The two layers remain in contact, but they are allowed to slide against each other with viscous friction. The viscous coefficient is evaluated by considering the distribution of transmembrane proteins (band 3 and glycophorin C) as well as their mobilities inside the lipid bilayer. Numerically, a nonlinear finite element approach[54] using continuum-based shell elements and penalty contact algorithms is employed to simulate the dynamics and interactions of both layers.[52] The constitutive properties of the cytoskeleton predicted by the Level II model are used in the Level III finite element model to calculate the Cauchy stress resultant of the inner layer as

$$\hat{\boldsymbol{\sigma}} = \tau_a(\alpha,\beta)\mathbf{I} + \frac{\mu(\alpha,\beta)}{(\alpha+1)^2}\left(\mathbf{B} - \frac{trace(\mathbf{B})}{2}\mathbf{I}\right), \tag{B4}$$

where τ_a and μ are the membrane mean stress resultant and shear modulus and calculated by Eq. (B3). $\mathbf{B} = \mathbf{G}\mathbf{G}^{\mathrm{T}}$ is the left Cauchy-Green deformation tensor.

In summary, in our multiscale framework, these three models are connected through a sequential information-passing technique:[11,52] The tabulated force-length curve of the spectrin monomer predicted by Eq. (B1) in the Level I model is used in the Level II model of the junctional complex to calculate the mean stress resultant and shear modulus in Eq. (B3) as two-variable tabulated functions of α and β. Then, these two-variable functions are used to calculate the Cauchy stress at the integration points of the shell elements for the cytoskeleton using Eq. (B4). The detailed parameters of the multiscale model are listed in Tables IV and V. The parameters of the cytoskeleton listed in Table V lead to an initial shear modulus $\mu_s = \mu(\alpha = 0, \beta = 0)$ of 7.5 pN/μm. We used the same set of parameters as we used in our previous studies such as RBCs in shear flows and tube flows.[11,18,53]

APPENDIX C: EFFECT OF SHARP CORNER SINGULARITIES AND VELOCITY/STRESS FIELDS IN THE MICROFLUIDIC SLIT

To illustrate the effect of sharp corner singularities and the mesh optimization technique employed in our simulation, we solved the velocity and stress distributions in the microfluidic slit and compared with the results from COMSOL Multiphysics.[80] The width of the narrow slit here is 0.8 μm, the length is 2.0 μm, and the depth is 5.0 μm. A pressure drop of 150 Pa is applied between the inlet and outlet. In COMSOL, an extremely fine mesh was used to ensure that the result is convergent.

Figures 14(a) and 14(b) are the velocity distributions on the middle plane from COMSOL and our numerical simulation, respectively. Figure 14(g) shows the velocity distributions along the x direction ($y = 0$) in the slit. We can clearly see that the velocity with mesh optimization is much closer to the COMSOL grid-converged solution, especially on the inlet part. The slightly discrepancy between the black curve and the red curve is because of the coarse mesh consisting of 3000 quadrilateral elements used in the boundary element method, in contrast to the 117 507 tetrahedral elements used in COMSOL.

The stress distributions of τ_{xx} and τ_{xy} from COMSOL are shown in Figs. 14(c) and 14(e), respectively. The corresponding solutions from our numerical simulation are shown in Figs. 14(d) and 14(f), respectively. Figure 14(h) gives the comparison of shear stress τ_{xy} along the y direction at the center of the slit between the COMSOL solution and our simulation. We can clearly see that the results from our simulations are very close to the COMSOL grid-converged solutions. The mesh optimization technique was employed in the simulations when we computed the stresses.

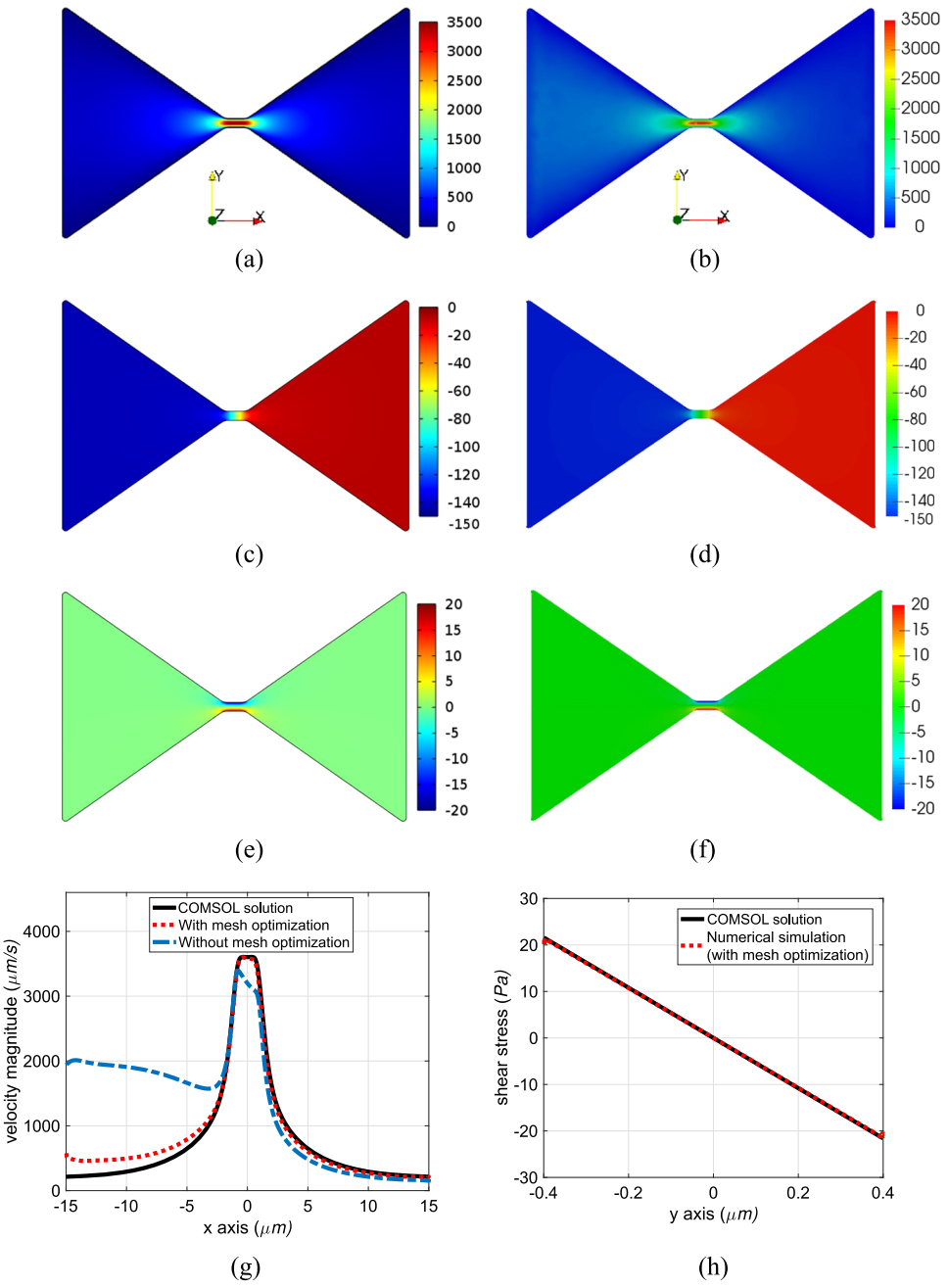

FIG. 14. Velocity and stress distributions on the middle plane in the domain. [(a) and (b)] Velocity distributions from COMSOL and current numerical simulation. Unit: μm/s. [(c) and (d)] τ_{xx} from COMSOL and current numerical simulation. Unit: Pa. [(e) and (f)] τ_{xy} from COMSOL and current numerical simulation. Unit: Pa. (g) Velocity along the x direction (y = 0) on the middle plane. (h) Shear stress τ_{xy} along the y direction (x = 0) on the middle plane. The origin of the xy coordinate system is set at the center of the slit.

REFERENCES

[1]D. Barthès-Biesel, "Motion and deformation of elastic capsules and vesicles in flow," Annu. Rev. Fluid. Mech. **48**, 25–52 (2016).

[2]J. B. Freund, "Numerical simulation of flowing blood cells," Annu. Rev. Fluid. Mech. **46**, 67–95 (2014).

[3]C. Pozrikidis, "Flow-induced deformation of two-dimensional biconcave capsules," in *Computational Hydrodynamics of Capsules and Biological Cells* (CRC Press, 2010), pp. 1–33.

[4]P. Perdikaris, L. Grinberg, and G. E. Karniadakis, "Multiscale modeling and simulation of brain blood flow," Phys. Fluids **28**, 021304 (2016).

[5]E. Kaliviotis, J. M. Sherwood, and S. Balabani, "Local viscosity distribution in bifurcating microfluidic blood flows," Phys. Fluids **30**, 030706 (2018).

[6]I. C. Tsimouri, P. S. Stephanou, and V. G. Mavrantzas, "A constitutive rheological model for agglomerating blood derived from nonequilibrium thermodynamics," Phys. Fluids **30**, 030710 (2018).

[7]J. Walter, A.-V. Salsac, D. Barthès-Biesel, and P. L. Tallec, "Coupling of finite element and boundary integral methods for a capsule in a Stokes flow," Int. J. Numer. Methods Eng. **83**, 829–850 (2010).

[8]C. Pozrikidis, *Boundary Integral and Singularity Methods for Linearized Viscous Flow* (Cambridge University Press, 1992).

[9]S. Kim and S. J. Karrila, *Microhydrodynamics: Principles and Selected Applications* (Butterworth-Heinemann, 1991).
[10]H. Zhao, A. H. Isfahani, L. N. Olson, and J. B. Freund, "A spectral boundary integral method for flowing blood cells," J. Comput. Phys. **229**, 3726–3744 (2010).
[11]Z. Peng, R. Asaro, and Q. Zhu, "Multiscale modeling of erythrocytes in Stokes flow," J. Fluid Mech. **686**, 299–337 (2011).
[12]P. Balogh and P. Bagchi, "Analysis of red blood cell partitioning at bifurcations in simulated microvascular networks," Phys. Fluids **30**, 051902 (2018).
[13]D. Cordasco and P. Bagchi, "On the shape memory of red blood cells," Phys. Fluids **29**, 041901 (2017).
[14]A. Yazdani, R. Kalluri, and P. Bagchi, "Tank-treading and tumbling frequencies of capsules and red blood cells," Phys. Rev. E **83**, 046305 (2011).
[15]Y. Liu and W. K. Liu, "Rheology of red blood cell aggregation by computer simulation," J. Comput. Phys. **220**, 139–154 (2006).
[16]Y. Sui, H. T. Low, Y. T. Chew, and P. Roy, "Tank-treading, swinging, and tumbling of liquid-filled elastic capsules in shear flow," Phys. Rev. E **77**, 016310 (2008).
[17]I. V. Pivkin and G. E. Karniadakis, "Accurate coarse-grained modeling of red blood cells," Phys. Rev. Lett. **101**, 118105 (2008).
[18]Z. Peng and Q. Zhu, "Deformation of the erythrocyte cytoskeleton in tank treading motions," Soft Matter **9**, 7617–7627 (2013).
[19]H. Noguchi, "Dynamic modes of red blood cells in oscillatory shear flow," Phys. Rev. E **81**, 061920 (2009).
[20]S. M. Hosseini and J. J. Feng, "How malaria parasites reduce the deformability of infected red blood cells," Biophys. J. **103**, 1–10 (2012).
[21]D. Discher, D. Boal, and S. Boey, "Simulations of the erythrocyte cytoskeleton at large deformation. II. Micropipette aspiration," Biophys. J. **75**, 1584–1597 (1998).
[22]Q. Du, C. Liu, and X. Wang, "A phase field approach in the numerical study of the elastic bending energy for vesicle membranes," J. Comput. Phys. **198**, 450–468 (2004).
[23]J. O. Barber, J. M. Restrepo, and T. W. Secomb, "Simulated red blood cell motion in microvessel bifurcations: Effects of cell–cell interactions on cell partitioning," Cardiovasc. Eng. Technol. **2**, 349–360 (2011).
[24]A. Ni, T. A. Cheema, and C. W. Park, "Numerical study of RBC motion and deformation through microcapillary in alcohol plasma solution," Open J. Fluid Dyn. **05**, 26–33 (2015).
[25]I. V. Pivkin, Z. Peng, G. E. Karniadakis, P. A. Buffet, M. Dao, and S. Suresh, "Biomechanics of red blood cells in human spleen and consequences for physiology and disease," Proc. Natl. Acad. Sci. U. S. A. **113**, 7804–7809 (2016).
[26]P. Gambhire, S. Atwell, C. Iss, F. Bedu, I. Ozerov, C. Badens, E. Helfer, A. Viallat, and A. Charrier, "High aspect ratio sub-micrometer channels using wet etching: Application to the dynamics of red blood cell transiting through biomimetic splenic slits," Small **13**, 1700967 (2017).
[27]H. Li, L. Lu, X. Li, P. A. Buffet, M. Dao, G. E. Karniadakis, and S. Suresh, "Mechanics of diseased red blood cells in human spleen and consequences for hereditary blood disorders," Proc. Natl. Acad. Sci. U. S. A. **115**, 9574–9579 (2018).
[28]I. Safeukui, P. A. Buffet, S. Perrot, A. Sauvanet, B. Aussilhou, S. Dokmak, A. Couvelard, D. C. Hatem, N. Mohandas, P. H. David, O. Mercereau-Puijalon, and G. Milon, "Surface area loss and increased sphericity account for the splenic entrapment of subpopulations of plasmodium falciparum ring-infected erythrocytes," PLoS ONE **8**, e60150 (2013).
[29]I. Safeukui, P. A. Buffet, G. Deplaine, S. Perrot, V. Brousse, A. Sauvanet, B. Aussilhou, S. Dokmak, A. Couvelard, D. Cazals-Hatem, O. Mercereau-Puijalon, G. Milon, P. H. David, and N. Mohandas, "Sensing of red blood cells with decreased membrane deformability by the human spleen," Blood Adv. **2**, 2581–2587 (2018).
[30]J. B. Freund, "The flow of red blood cells through a narrow spleen-like slit," Phys. Fluids **25**, 110807 (2013).
[31]S. Salehyar and Q. Zhu, "Deformation and internal stress in a red blood cell as it is driven through a slit by an incoming flow," Soft Matter **12**, 3156–3164 (2016).
[32]Q. Zhu, S. Salehyar, P. Cabrales, and R. J. Asaro, "Prospects for human erythrocyte skeleton-bilayer dissociation during splenic flow," Biophys. J. **113**, 900–912 (2017).
[33]R. E. Mebius and G. Kraal, "Structure and function of the spleen," Nat. Rev. Immunol. **5**, 606–616 (2005).
[34]G. Deplaine, I. Safeukui, F. Jeddi, F. Lacoste, V. Brousse, S. Perrot, S. Biligui, M. Guillotte, C. Guitton, S. Dokmak, B. Aussilhou, A. Sauvanet, A. Couvelard, F. Paye, M. Thellier, D. Mazier, G. Milon, N. Mohandas, O. Puijalon, P. H. David, and P. A. Buffet, "A micro-bead device to explore plasmodium falciparum-infected, spherocytic or aged red blood cells prone to mechanical retention by spleen endothelial slits," Malar. J. **9**, O10 (2010).
[35]N. Mohandas and P. G. Gallagher, "Red cell membrane: Past, present, and future," Blood **112**, 3939–3948 (2008).
[36]S. Salehyar and Q. Zhu, "Effects of stiffness and volume on the transit time of an erythrocyte through a slit," Biomech. Model. Mechanobiol. **16**, 921–931 (2016).
[37]G. Deplaine, I. Safeukui, F. Jeddi, F. Lacoste, V. Brousse, S. Perrot, S. Biligui, M. Guillotte, C. Guitton, S. Dokmak, B. Aussilhou, A. Sauvanet, D. C. Hatem, F. Paye, M. Thellier, D. Mazier, G. Milon, N. Mohandas, O. Mercereau-Puijalon, P. H. David, and P. A. Buffet, "The sensing of poorly deformable red blood cells by the human spleen can be mimicked *in vitro*," Blood **117**, e88–e95 (2010).
[38]I. Safeukui, P. A. Buffet, G. Deplaine, S. Perrot, V. Brousse, A. Ndour, M. Nguyen, O. Mercereau-Puijalon, P. H. David, G. Milon, and N. Mohandas, "Quantitative assessment of sensing and sequestration of spherocytic erythrocytes by the human spleen," Blood **120**, 424 (2012).
[39]C. Pozrikidis, "Numerical simulation of cell motion in tube flow," Ann. Biomed. Eng. **33**, 165–178 (2005).
[40]S. Kuriakose and P. Dimitrakopoulos, "Motion of an elastic capsule in a square microfluidic channel," Phys. Rev. E **84**, 011906 (2011).
[41]S.-Y. Park and P. Dimitrakopoulos, "Transient dynamics of an elastic capsule in a microfluidic constriction," Soft Matter **9**, 8844 (2013).
[42]A. Koolivand and P. Dimitrakopoulos, "Deformation of an elastic capsule in a microfluidic T-junction: Settling shape and moduli determination," Microfluid. Nanofluid. **21**, 89 (2017).
[43]A. Leyrat-Maurin and D. Barthès-Biesel, "Motion of a deformable capsule through a hyperbolic constriction," J. Fluid Mech. **279**, 135 (1994).
[44]A. Leyrat-Maurin, A. Drochon, A. Leverger, and D. Barthès-Biesel, "Effect of geometry and membrane properties on the flow of capsules through a short pore at constant pressure drop," Biorheology **32**, 312–313 (1995).
[45]J. Happel and H. Brenner, *Low Reynolds Number Hydrodynamics* (Springer Netherlands, 1981).
[46]J. Telles, "A self-adaptive co-ordinate transformation for efficient numerical evaluation of general boundary element integrals," Int. J. Numer. Methods Eng. **24**, 959–973 (1987).
[47]S. Weinbaum, P. Ganatos, and Z. Yan, "Numerical multipole and boundary integral equation techniques in Stokes flow," Annu. Rev. Fluid Mech. **22**, 275–316 (1990).
[48]B. Neu, S. O. Sowemimo-Coker, and H. J. Meiselman, "Cell-cell affinity of senescent human erythrocytes," Biophys. J. **85**, 75–84 (2003).
[49]M. Rasia and A. Bollini, "Red blood cell shape as a function of medium's ionic strength and pH," Biochim. Biophys. Acta, Biomembr. **1372**, 198–204 (1998).
[50]S. Weinbaum, J. M. Tarbell, and E. R. Damiano, "The structure and function of the endothelial glycocalyx layer," Annu. Rev. Biomed. Eng. **9**, 121–167 (2007).
[51]C. Pozrikidis, "Boundary element grid optimization for Stokes flow with corner singularities," J. Fluids Eng. **124**, 22 (2002).
[52]Z. Peng, R. Asaro, and Q. Zhu, "Multiscale simulation of erythrocyte membranes," Phys. Rev. E **81**, 031904 (2010).
[53]Z. Peng, A. Mashayekh, and Q. Zhu, "Erythrocyte responses in low shear rate flows–Effects of non-biconcave stress-free state in cytoskeleton," J. Fluid Mech. **742**, 96–118 (2014).
[54]T. Belytschko, W. Liu, and B. Moran, *Nonlinear Finite Elements for Continua and Structures* (John Wiley, New York, 2000).

[55]Z. Peng, S. Salehyar, and Q. Zhu, "Stability of the tank treading modes of erythrocytes and its dependence on cytoskeleton reference states," J. Fluid Mech. **771**, 449–467 (2015).
[56]M. Abkarian, M. Faivre, and A. Viallat, "Swinging of red blood cells under shear flow," Phys. Rev. Lett. **98**, 188302 (2007).
[57]W. Yao, Z. Wen, Z. Yan, D. Sun, W. Ka, L. Xie, and S. Chien, "Low viscosity ektacytometry and its validation tested by flow chamber," J. Biomech. **34**, 1501–1509 (2001).
[58]Q. Zhu and R. Asaro, "Spectrin folding vs. unfolding reactions and RBC membrane stiffness," Biophys. J. **94**, 2529–2545 (2008).
[59]R. Skalak, A. Tozeren, R. P. Zarda, and S. Chien, "Strain energy function of red blood cell membranes," Biophys. J. **13**(3), 245–264 (1973).
[60]E. Evans and P. Skalak, *Mechanics and Thermodynamics of Biomembranes* (CRC Press, Boca Raton, FL, 1980).
[61]M. Dao, J. Li, and S. Suresh, "Molecularly based analysis of deformation of spectrin network and human erythrocyte," Mater. Sci. Eng.: C **26**, 1232–1244 (2006).
[62]J. Li, M. Dao, C. T. Lim, and S. Suresh, "Spectrin-level modeling of the cytoskeleton and optical tweezers stretching of the erythrocyte," Biophys. J. **88**, 3707–3719 (2005).
[63]G. Závodszky, B. van Rooij, V. Azizi, and A. Hoekstra, "Cellular level *in-silico* modeling of blood rheology with an improved material model for red blood cells," Front. Physiol. **8**, 563 (2017).
[64]S. K. Boey, D. H. Boal, and D. E. Discher, "Simulations of the erythrocyte cytoskeleton at large deformation. I. Microscopic models," Biophys. J. **75**, 1573–1583 (1998).
[65]J. Li, G. Lykotrafitis, M. Dao, and S. Suresh, "Cytoskeletal dynamics of human erythrocyte," Proc. Natl. Acad. Sci. U. S. A. **104**, 4937–4942 (2007).
[66]H. Li and G. Lykotrafitis, "Erythrocyte membrane model with explicit description of the lipid bilayer and the spectrin network," Biophys. J. **107**, 642–653 (2014).
[67]S.-P. Fu, Z. Peng, H. Yuan, R. Kfoury, and Y.-N. Young, "Lennard-Jones type pair-potential method for coarse-grained lipid bilayer membrane simulations in LAMMPS," Comput. Phys. Commun. **210**, 193–203 (2017).
[68]W. Pan, B. Caswell, and G. E. Karniadakis, "A low-dimensional model for the red blood cell," Soft Matter **6**(18), 4366 (2010).
[69]D. J. Jeffrey, "Low-Reynolds-number flow between converging spheres," Mathematika **29**, 58–66 (1982).
[70]P. Gambhire, S. Atwell, C. Iss, F. Bedu, I. Ozerov, C. Badens, E. Helfer, A. Viallat, and A. Charrier, "Dynamics of red blood cells transiting through biomimetic splenic slits" (unpublished raw data).
[71]S. M. Cahalan, V. Lukacs, S. S. Ranade, S. Chien, M. Bandell, and A. Patapoutian, "Piezo1 links mechanical forces to red blood cell volume," eLife **4**, e07370 (2015).
[72]Z. Peng, O. S. Pak, Z. Feng, A. P. Liu, and Y.-N. Young, "On the gating of mechanosensitive channels by fluid shear stress," Acta Mech. Sin. **32**, 1012–1022 (2016).
[73]D. Boal, *Mechanics of the Cell*, 2nd ed. (Cambridge University Press, 2012).
[74]N. Mohandas and E. A. Evans, "Mechanical properties of the red cell membrane in relation to molecular structure and genetic defects," Annu. Rev. Biophys. Biomol. Struct. **23**, 787–818 (1994).
[75]M. Dao, C. Lim, and S. Suresh, "Mechanics of the human red blood cell deformed by optical tweezers," J. Mech. Phys. Solids **51**, 2259–2280 (2003).
[76]M. Brust, C. Schaefer, R. Doerr, L. Pan, M. Garcia, P. E. Arratia, and C. Wagner, "Rheology of human blood plasma: Viscoelastic versus Newtonian behavior," Phys. Rev. Lett. **110**, 078305 (2013).
[77]S. Varchanis, Y. Dimakopoulos, C. Wagner, and J. Tsamopoulos, "How viscoelastic is human blood plasma?," Soft Matter **14**, 4238–4251 (2018).
[78]K. Luby-Phelps, "Cytoarchitecture and physical properties of cytoplasm: Volume, viscosity, diffusion, intracellular surface area," in *International Review of Cytology* (Elsevier, 1999), pp. 189–221.
[79]R. P. Sear, "The cytoplasm of living cells: A functional mixture of thousands of components," J. Phys.: Condens. Matter **17**, S3587–S3595 (2005).
[80]See http://www.comsol.com for COMSOL Multiphysics Reference Manual, version 5.3, COMSOL, Inc.